

UNIVERSIDADE FEDERAL DO RIO GRANDE DO SUL
INSTITUTO DE INFORMÁTICA
PROGRAMA DE PÓS-GRADUAÇÃO EM COMPUTAÇÃO

CLEÓBULO SALES NETO

**A Portable and Low-Cost Corneal
Topographer Design**

Thesis presented in partial fulfillment
of the requirements for the degree of
Master of Computer Science

Advisor: Prof. Dr. Manuel Menezes de Oliveira
Neto

Legal Notice

Thesis defended on 21 December 2015 in private session with legal confidentiality agreement between parties. For all legal purposes this full text is not publicly available until the publication date on 21 December 2017.

Aviso

Tese defendida em 21/12/2015 em sessão privada sob acordo de sigilo entre as partes. Publicação do texto da tese em 21/12/2017. Para todos os fins legais este texto se tornou publico em 21/12/2017, não estando disponível publicamente antes desta data.

Porto Alegre

CIP — CATALOGING-IN-PUBLICATION

Sales Neto, Cleóbulo

A Portable and Low-Cost Corneal Topographer Design /
Cleóbulo Sales Neto. – Porto Alegre: PPGC da UFRGS, .

95 f.: il.

Thesis (Master) – Universidade Federal do Rio Grande do Sul.
Programa de Pós-Graduação em Computação, Porto Alegre, BR–
RS, . Advisor: Manuel Menezes de Oliveira Neto.

1. Corneal Topography. 2. Eye Health. 3. Computational Pho-
tography. I. de Oliveira Neto, Manuel Menezes. II. Título.

UNIVERSIDADE FEDERAL DO RIO GRANDE DO SUL

Reitor: Prof. Carlos Alexandre Netto

Vice-Reitor: Prof. Rui Vicente Oppermann

Pró-Reitor de Pós-Graduação: Prof. Vladimir Pinheiro do Nascimento

Diretor do Instituto de Informática: Prof. Luis da Cunha Lamb

Coordenador do PPGC: Prof. Luigi Carro

Bibliotecária-chefe do Instituto de Informática: Beatriz Regina Bastos Haro

“Research is what I’m doing when I don’t know what I’m doing.”

— WERNHER VON BRAUN

ABSTRACT

Corneal topography is an important tool for understanding and assessing one's visual acuity. However, acquiring this information is not simple, and normally requires an instrument called corneal topographer. In this thesis, we present an in-depth pipeline for building a portable and low-cost corneal topographer. We present an investigation and a discussion about the major steps of its construction using software simulations and empirical trials. We present a simple and easily reproducible design that we have used to build a physical prototype. Although fairly inexpensive, our prototype provides useful topography data that can be of special interest for screening purposes. The proposed pipeline shall be easily reproduced by those interested in going even further in the investigation of corneal topography, or just wanting to build their own portable and low-cost corneal topographer. We evaluate our prototype's performance using our simulation environment and comparing its performance against existing devices.

Keywords: Corneal Topography. Eye Health. Computational Photography.

Topografia de Córnea de Baixo Custo

RESUMO

Topografia de córnea é uma importante ferramenta para o entendimento e avaliação da acuidade visual de um indivíduo. No entanto, a aquisição desse tipo de informação não é simples e requer o uso de um instrumento conhecido como topógrafo de córnea. Nessa dissertação, apresentamos uma investigação sobre os principais passos de sua construção usando simulações em software e testes empíricos. No apresentamos um design simples e fácil de reproduzir que nós usamos para construir um protótipo físico. Embora de baixo custo, nosso protótipo provê informação topográfica útil e que tem especial potencial para processos de triagem. Propomos uma sequência de etapas que deverá ser facilmente reproduzida por aqueles interessados em ir ainda mais além na investigação da topografia de córnea, or apenas estão desejando construir o seu próprio topógrafo de córnea portátil e de baixo custo. Nós avaliamos a performance do nosso protótipo usando nosso ambiente de simulação em software e comparando sua performance em relação a de soluções comerciais existentes.

Palavras-chave: Topografia de Córnea. Acuidade Visual. Saúde Visual.

LIST OF FIGURES

Figure 1.1	Different corneal assessments throughout time.	15
Figure 1.2	Examples of portable and low-cost visual acuity assessment.	16
Figure 2.1	Cross section of the human eye.	20
Figure 2.2	A Placido-based-system and its assessment.	23
Figure 2.3	Examples of images captured by a Placido-disk-based system. (a) A healthy and regular cornea. (b) A cornea with keratoconus.	24
Figure 2.4	A simplified two dimensional corneal surface reconstruction problem schema.....	24
Figure 2.5	Hierarchical ladder of corneal height, slope, and curvature, and the conversion between steps. Axial power is related to the slope data and the curvature of the cornea.	26
Figure 2.6	An example of axial curvature map.	29
Figure 3.1	Schema represents the process of visual assessment using NETRA and the result on a smartphone screen.	31
Figure 3.2	Cataract assessment using slit lamp on the left and CATRA on the right.	32
Figure 3.3	Visual acuity assessment in small children using eye tracking.	32
Figure 3.4	Comparison of retinal images obtained using PEEK and a commercial device.	33
Figure 3.5	A corneal topographer for palm device and the results obtained using it. ...	34
Figure 3.6	The corneal topographer prototype proposed by Rosa ().	34
Figure 3.7	The corneal topographer developed by Pinheiro et al. () and the process of assessment using it.....	35
Figure 4.1	Input data acquisition scheme.....	37
Figure 4.2	Axial curvature color map generated by Topcon KR-8000PA.	39
Figure 4.3	Simple portable topographer design.	39
Figure 4.4	Topographer simplified scheme.	40
Figure 4.5	Ellipsotoric model in cylindrical coordinates.	43
Figure 4.6	Our corneal surface simulation software.	43
Figure 4.7	Relation between the meridians from the surface and on the sensor plane. ...	45
Figure 4.8	Equivalences between the cartesian and cylindrical coordinates.	47
Figure 4.9	Ellipsotoric model in cylindrical coordinates.	47
Figure 4.10	Radial sampling for two different surfaces.....	49
Figure 4.11	Result from General Sampling.	51
Figure 4.12	Corneal Topographer Chroma by Wavetek.....	52
Figure 4.13	Surface reflecting the Placido Disk pattern.	53
Figure 4.14	Two regions of transition distribution over the same profile	53
Figure 4.15	Schema illustrating the blind spot.	55
Figure 4.16	Our controlled pattern creation software.	57
Figure 4.17	Variety of color scales.....	60
Figure 4.18	Color map for simulated subject.....	60
Figure 4.19	Representations of the corneal area covered by videokeratoscope and the keratometer.....	61
Figure 5.1	Prototype outer shell.....	64
Figure 5.2	Prototype outer shell.....	65
Figure 5.3	Outer shell case.....	65

Figure 5.4 Outer shell components assembling.	66
Figure 5.5 Outer shell case lid.	66
Figure 5.6 Outer shell core and its components.	67
Figure 5.7 The cone.	68
Figure 5.8 The cone blueprint creation process.	68
Figure 5.9 Cone blueprint properties and truncated cone schemas.	69
Figure 5.10 Cone blueprint and actual printed and folded cone patterns.	70
Figure 5.11 Calibration spheres used.	71
Figure 5.12 Two color maps for the same data with different sampling density.	74
Figure 5.13 Segmentation needed for simulated keratometry.	75
Figure 6.1 Imaging of three simulated spheres.	78
Figure 6.2 Average K values obtained from the reconstruction of the simulated spheres varying the imaging distance.	79
Figure 6.3 Three simulated subjects with astigmatism.	80
Figure 6.4 The color maps for the subjects A, B and C.	80
Figure 6.5 Color maps for the reconstructed synthetic cases.	82
Figure 6.6 The acquisition process and the segmentation used.	84
Figure 6.7 Difference maps derived from the color maps generated by our prototype. .	85
Figure 6.8 Color maps generated by our prototype compared to their respective reference map.	86
Figure 6.9 Main radius-of-curvature reconstruction error for 12 human subjects.	88
Figure 6.10 Main axial-curvatures reconstructions error for 12 human subjects.	89
Figure 6.11 Astigmatism error estimation for human subjects.	90

LIST OF TABLES

Table 6.1	Reconstruction of simulated spheres.....	77
Table 6.2	Reconstructed values for simulated subjects with $S_f = 0.9$	78
Table 6.3	K value reconstruction for astigmatic simulated subjects with non-neutral value of shape factor.	80
Table 6.4	K values reconstructed for the calibration spheres.....	81

CONTENTS

1 INTRODUCTION	15
1.1 Thesis Structure	17
2 CORNEAL TOPOGRAPHY	19
2.1 The Human Eye	19
2.1.1 Cornea	20
2.2 History of Corneal Measurements	20
2.3 Corneal Topographers	22
2.3.1 Placido Disk based Corneal Topographers	23
2.4 Surface Reconstruction Problem	24
2.4.1 The Skew Ray Error	27
2.4.2 Corneal Topography Main Issues	27
2.5 Data Visualization	28
3 RELATED WORKS	31
3.1 Visual Acuity Assessment	31
3.2 Portable And Low-Cost Corneal Topography	33
4 A LOW-COST CORNEAL-TOPOGRAPHY APPROACH	37
4.1 Corneal Topography Pipeline	37
4.1.1 Corneal Topographer Design	40
4.2 The Corneal Topography Simulation	41
4.2.1 Modeling the Corneal Surface	41
4.2.2 Simulating a Topographer System	42
4.3 Imaging the Simulated Cornea	44
4.3.1 Radial Sampling	45
4.3.2 General Sampling	48
4.4 Crafting a Corneal Pattern Through Simulation	51
4.4.1 Pattern Creation using Inverse Sampling	53
4.4.1.1 Calculating the Arcs.....	54
4.4.1.2 The Blind Spot	55
4.4.1.3 Building the Pattern	56
4.4.1.4 Inverse Sampling Summary	56
4.5 Surface Data Reconstruction	56
4.6 High-Level Data Extraction	59
4.6.1 Color Maps.....	59
4.6.2 Simulated Keratometry	59
5 THE CREATION OF A PROTOTYPE	63
5.1 The Corneal Topographer Device	63
5.1.1 The Outer Shell	64
5.1.2 The Cone	66
5.1.3 The Light Source.....	69
5.2 Imaging Corneal Surfaces	70
5.3 Image Segmentation	71
5.3.1 Computing the Center of the Reflected Pattern	72
5.4 Prototype Output	73
6 RESULTS	77
6.1 Virtual Subjects	77
6.2 Synthetic Subjects	81
6.3 Human Subjects	82
6.3.1 Color Maps Comparison	83

6.3.2 Simulated Keratometry Evaluation.....	87
7 CONCLUSIONS AND FUTURE WORK.....	91
7.1 Future Work	92
REFERENCES.....	93

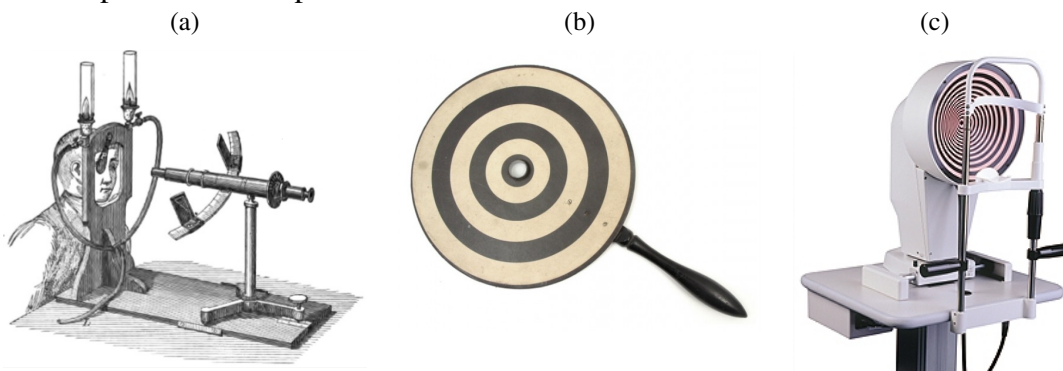
1 INTRODUCTION

World Health Organization¹ (WHO) estimates that there are 285 millions of people visually impaired worldwide, 39 millions of them being blind. Around 90% of the visually impaired people live in low-income environments. WHO also estimates that 80% of all visual impairment can be prevented or cured.

The cornea is a fundamental piece of the human visual system, besides being the only transparent external surface in the whole human body. It holds around 67% of all eye's refractive power, and this is mostly defined by its geometry. Therefore, assessing one's corneal geometry provides important and useful information about one's visual acuity. Moreover, it is the best way to detect sets of particular conditions, such as keratoconus which causes major harm to one's vision.

Many technical approaches have been developed for corneal assessment. The oldest procedure dates back to 19th century, consisting on measuring the corneal main curvatures. The assessment was done by a tool known as *keratometer* (Figure 1.1(a)), which gives the name for the procedure: keratometry. It uses the reflection of patterns on the corneal surface to estimate main corneal curvatures (Figure 1.1(a)). The advent of new technologies during the 20th century, especially the appearance of photographic cameras, enabled the creation of new and distinct methods for performing the assessment of this information.

Figure 1.1: Different corneal assessments throughout time. (a) one of the first keratometers, designed by Javal-Schiøtz, (b) the original design for a Placido-disk hand-held device, (c) a modern photokeratoscope based on the Placido disk.



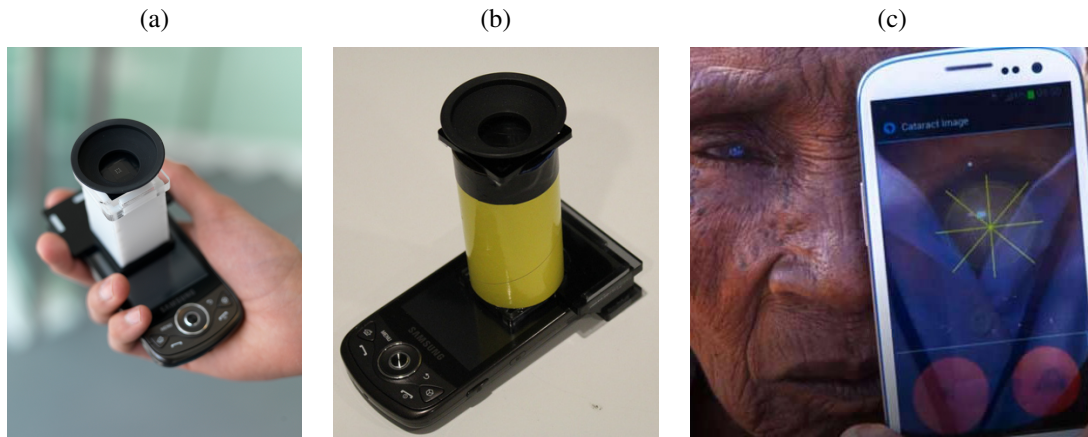
Source: Source: (a) Gutmark and Guyton (), (b)Phisick², (c) News Medical³.

¹<http://www.who.int> (Last visited 11/09/2015)

²<http://www.phisick.com/> (Last visited 11/09/2015)

³<http://www.news-medical.net/> (Last visited 5/12/2015)

Figure 1.2: Examples of portable and low-cost visual acuity assessment. (a) a prototype for refractive error assessment NETRA, (b) a prototype for cataract assessment CATRA and (c) the software application PEEK.



Source: Source: (a) Pamplona et al. (a) (b) Pamplona et al. (b) (c) PEEK's website³.

The *photokeratoscope* was created based on the keratometer ideas and a simple tool developed by the Portuguese ophthalmologist Antônio Plácido (PLÁCIDO,) (Figure 1.1(b)). Later on, with the advent of video recording devices, the videokeratographs were created and used till nowadays, being known as corneal topographers (Figure 1.1(c)).

Corneal topographers are one of the most modern and specialized tools in assessing corneal geometry information. They can be used for visual acuity assessment, for lens fitting, intra-surgical assessment, and for a myriad of other ophthalmologic applications. However, a corneal topographer usually consists of specific and dedicated hardware, which tends to be very expensive. Its price is a limiting factor, which makes it not affordable on many places, specially on emerging countries and remote areas.

There is a current trend of using the computational power of hand-held devices, such as smartphones, to provide portable and low-cost visual health assessment. Some examples of such endeavors are NETRA (PAMPLONA et al., a), CATRA (PAMPLONA et al., b) and PEEK⁴. They can be seen in Figure 1.2. On this work, we investigate the construction of a portable low-cost corneal topographer using a smartphone. We present a thorough process for building such a device with a limited budget.

We start by presenting our corneal topography pipeline. It helps us to better understand how a corneal topographer works, while also being able to modularly incorporate available works regarding corneal topography. We validate this pipeline using software simulation to assess virtual subjects.

In order to create our software simulation, we developed *Radial Sampling* and

⁴<http://www.peakvision.org/> (Last visited 11/09/2015)

General Sampling approaches to simulate the process of imaging a subject represented by a mathematical model. Also, we propose an *Inverse Sampling* technique in order to design controlled patterns, which allows for arbitrary spatial distribution of samples on target surfaces.

Finally, we present a physical prototype of our portable low-cost corneal topographer. We discuss its building process and the problems regarding noisy inputs. Additionally, we compare its results against ones obtained by traditional commercial topographers.

The **contributions** of this thesis include:

- To our knowledge, the first documented non-proprietary *Topography Pipeline* that consists of a series of stages to be performed in order to extract one's corneal data. Our model can be used to incorporate available techniques for different stages of the corneal assessment;
- The creation of a simulation environment to perform corneal assessment on virtual subjects defined by mathematical models (e.g., ellipsotopic model). On top of it, we present the approaches: *Radial Sampling* and the *General Sampling* which are different approaches to solve the corneal assessment simulation.
- An *Inverse Sampling* technique which can be used to calculate arbitrary Placido Disk patterns. It allows one to have better control over the reflection of a pattern on a subject's cornea, hence being able to influence the sampling spatial distribution on a subject;
- The presentation of an original *physical portable and low-cost corneal topographer prototype*. We provide reproducible guidelines for those interested in building their own topographer;

1.1 Thesis Structure

The remaining of this thesis is organized as follows: Chapter 2 presents a theoretical background related to corneal topography. Chapter 3 presents related work, focusing on successful endeavors in visual health evaluation using hand-held devices. In Chapter 4, we present our topography pipeline and our approach to simulate a subject imaging process. Also, we present our *Inverse Sampling* process. Chapter 5 presents a physical prototype and major technical issues related to the process of building it. In Chapter 6, we present our results, comparing them against a commercial solutions. Finally, in Chapter 7

we summarize our work, discussing main concerns and directions for further exploration.

2 CORNEAL TOPOGRAPHY

Corneal topography provides very useful information for optometrists and ophthalmologists, since it assesses the cornea's shape. Specially important for detecting keratoconus, a rare condition known to have huge impact in one's visual acuity. In this chapter, we establish and review some of the theoretical principles regarding corneal topography that are important for the construction of our portable low-cost prototype, data analysis, and interpretation of the results.

2.1 The Human Eye

The eye is the structure of the human visual system responsible for properly capturing the light stimuli from the environment and focusing it on an innermost surface called retina. In order to do so, it relies on a complex optical system comprised by the cornea, the aqueous humor, the crystalline lens, and the vitreous humor. A cross section of the eye may be seen in Figure 2.1.

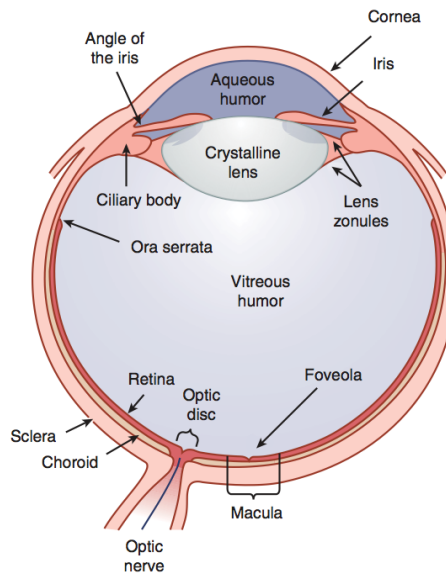
Structurally, the eye is composed of three concentric layers. From the outermost to the innermost, they are the sclera, the uvea and the retina. The sclera is mainly responsible for support and protection for the internal elements of the eye. The uvea is a highly vascularized layer which consists of iris, ciliary body, and choroid. The retina (where image formation occurs) is an exceedingly complex multi-layered neural element only 0.2 mm thick (SCHWARTZ,).

Within the iris there are muscles that control the diameter of the pupil, therefore regulating the amount of light entering the eye. The ciliary body contains muscles that are responsible for contracting the crystalline lens for near vision, this process is known as accommodation. It is also responsible for the production of aqueous humor. The choroid provides blood supply to the outer retina.

The crystalline lens are posterior to the iris and holds $1/3$ of the eye's refractive power (around 20 diopters)(SCHWARTZ,). However due to the accommodation, its optical power may change, thus allowing the eye to focus at different depths.

The aqueous and vitreous humors are gel-like fluids that contribute mostly to maintain eye structure and have little influence on the refractive power of the eye's optical system.

Figure 2.1: Cross section of the human eye.



Source: Schwartz ()

2.1.1 Cornea

The cornea is the most external structure of the eye's optical system. It holds 2/3 of all eye's refractive power (about 40 diopters). It is a circular, multi-layered, transparent, avascular tissue (approximately 0.55 mm thick at its apex and 12 mm in diameter) (APPLEGATE R.; HOWLAND,). The cornea is normally covered by a thin layer of tears usually referred to as *tear film*, which is mainly responsible for the eye's specular reflection.

Its geometry has fundamental importance on how the light will focus on the retina. Thus, naturally or induced (e.g., a cornea that has undergone surgery) abnormal shapes may introduce several and sometimes hard to predict effects. These effects are often referred to as aberrations. Cornea's shape may cause conditions like astigmatism, which is characterized by a discrepancy between the main curvatures of the surface. Also, irregular deviations spread over the corneal surface may lead to conditions like keratoconus, which may affect severely one's visual acuity and is hard to detect at the early stages.

2.2 History of Corneal Measurements

Keratometry was once the field of ophthalmology focused on obtaining the main curvatures of the surface of the cornea. Creating a device capable of extracting such in-

formation dates back to more than 200 years. It is called *keratometer* or *ophthalmometer*.

In 1796, Jesse Ramsden built a telescope in order to amplify images reflected on the external surface of the cornea, this was first described some years early by Ramsden and Banks (). He was investigating if the cornea's curvature changed during the process known as accommodation. He developed the core ideas for keratometry, many of them are still used by modern keratometers.

In 1854 Hermann von Helmholtz unified the work done by Ramsden and some other researchers like the astronomer Clausen to build a keratometer with adjustable mires. Helmholtz is often credited with the invention of the keratometer.

Two main principles were fundamental for this keratometer: the first one was assuming the cornea to be a spherical reflecting surface whose curvature could be calculated by measuring the reflection of an object of known size at a known distance. And the second one was that the image-doubling concept provided accurate measurements despite of the eye's and the head movements. Those two main principles remained mostly unchanged and were used for most keratometers.

For some time, keratometers remained as a laboratory instrument until Louis Émile Javal and Hjalmar August Schiøtz, in 1881, adapted it to be used at clinical practice. Also, they changed the instrument in a way one could choose in which axis the measurement of the curvature would be performed. Those instruments would later be called as Javal-Schiøtz's keratometer.

In 1880, the portuguese ophthalmologist Antônio Plácido developed an instrument which helped him in making a more general and qualitative measurement of one's visual acuity (PLÁCIDO,). He proposed a device composed of a series of concentric rings with a central hole. The evaluation of a subject was done by looking through the center hole to see how was the reflection of the concentric rings on the surface of the subject's eye. The pattern of concentric circles used is usually referred to as Placido disk.

Finally in 1896, Gullstrand attached a photo camera to Placido's device originating the photokeratoscope. Which led to more mathematically based analysis of the pattern's reflection which provided more quantitative measurements of the cornea's surface. In the 1970's, photokeratoscopes were designed to have Polaroid cameras attached. Although many advances had been made in this technology, it was not widely accepted among clinicians which still relied on the more familiar and traditional keratometer. Keratometry was often restricted to advanced contact lens fitting.

It was during the 1980's with the popularization of keratorefractive surgery that

keratoscope become more important and popular for clinical practice. One decade later, a new generation of keratoscopes was going to be designed as modern computerized systems attached with video cameras capable of taking pictures of high quality and analysing them, thus providing more robust cornea's measurement. Modern video keratoscope are used until today and are usually referred to as corneal topographers.

2.3 Corneal Topographers

Corneal topographers are the devices specialized in acquiring a corneal surface description. There are many kinds of topographers, they are classified according to the physical phenomena they rely on to infer relief information. Each one of these being more adequate for specific purposes and budgets.

Following the classification of topographers proposed by Yobani and Daniel (), we may group topographers in 3 major categories: specular reflection, diffuse reflection and scattered light. This classification covers the most used and more popular corneal topography principles.

Relying on the specular reflection of the cornea there are systems based on the Placido disk, interferometry techniques, and moiré deflectometry. Placido disk based systems are probably the older (JONGSMA; BRABANDER; HENDRIKSE,), simpler and most widespread kind of commercial topographer (APPLEGATE R.; HOWLAND,). Interferometry techniques extract corneal topography data from the interference pattern formed by the corneal reflection of a monochromatic coherent light beam (APPLEGATE R.; HOWLAND,). Although sub-micron precision is possible, its a very sensitive to calibration and has not yet found its way into daily clinical practice. Nevertheless, interferometry techniques are widely used to evaluate optical elements as lenses and mirrors (YOBANI; DANIEL,). In systems based on the moiré deflectometry, the deflection of collimated rays reflected on the surface of the cornea is analysed (YOBANI; DANIEL,).

In order to benefit from diffuse reflection for corneal topography, one must first turn the surface of the cornea into a diffuse surface. This is done by instilling fluorescein on the tear film. Once the cornea has diffuse reflection, structured light patterns might be projected and usual methods for measuring the resulting distortion over diffuse surfaces may be used (YOBANI; DANIEL,). Rasterstereography system rely on this physical phenomena to work. Although being quite invasive, topographers based on diffuse reflection

Figure 2.2: A Placido-based-system and its assessment. (a) The corneal topographer Topcon-8000PA. (b) An example of corneal assessment done by this kind of device.



Source: Source: (a) Topcon's website (b) Zamarripa Opticos's website.

may often get information from all corneal anterior surface.

And the last group of topographers is the one containing the ones that rely on the scattering phenomenon of light when it is transmitted in an optical medium. Basically, it uses the corneal tissue as the optical medium where the light is scattered. The light that emerges through the anterior surface of the cornea is captured by an imaging device. By using this method it is possible to measure both sides of the cornea (other methods can only measure the anterior surface). Slitlamp systems belong to this group.

2.3.1 Placido Disk based Corneal Topographers

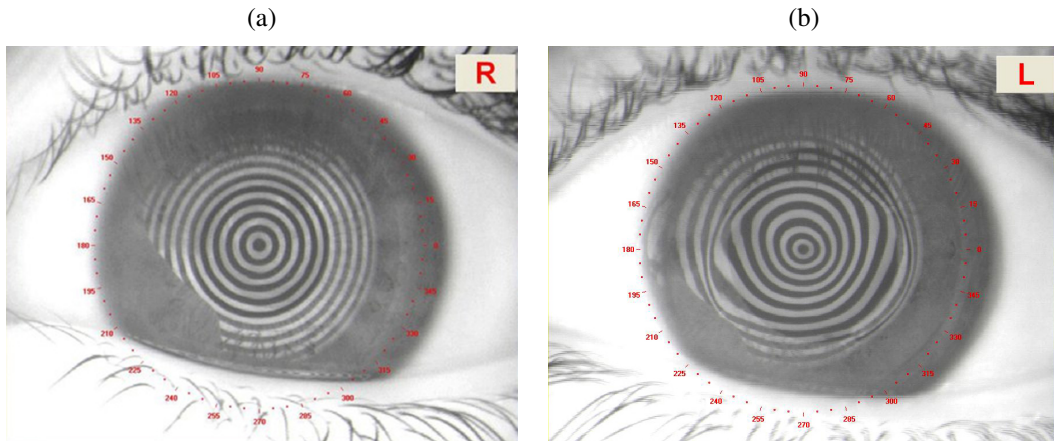
The assessment done by Placido-disk-based devices is straightforward. Figure 2.2(a) illustrates a modern placido-disk-based topographer the Topcon-8000PA¹ which was used to provide reference corneal data during the development of this thesis. Figure 2.2(b) illustrates the assessment done by this kind of device².

This kind of devices capture images of the corneal surface with the reflection of the concentric circles from the Placido disk pattern (Figure 2.3). From such an image, the surface data is reconstructed. It is important to note that there are multiple approaches to retrieve this data from the captured image. Moreover, different commercial devices will often include additional tools to enhance the assessments. For instance, the Topcon-8000PA also have tools to perform as an auto keratometer or an auto refractor.

¹<http://www.topconmedical.com/> (Last visited 12/12/2015)

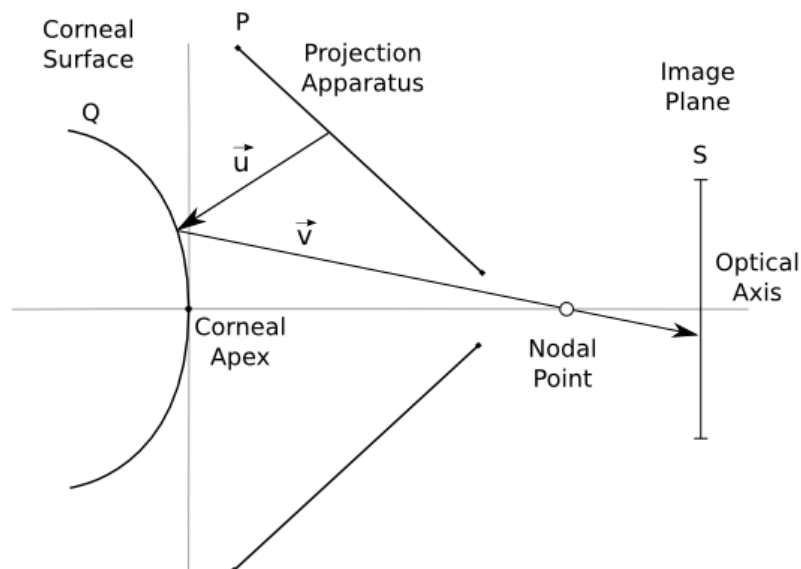
²The image was not obtained by using the Topcon-8000PA, instead it was taken from the Zamarripa Optico's website: <http://www.zamarripa.es/> (Last visited 12/12/2015)

Figure 2.3: Examples of images captured by a Placido-disk-based system. (a) A healthy and regular cornea. (b) A cornea with keratoconus.



Source: Source: Zamarripa Opticos's website.

Figure 2.4: A simplified two dimensional corneal surface reconstruction problem schema.



Source: the authors.

2.4 Surface Reconstruction Problem

The first step to understand corneal topographers is to know what is the exactly theoretical problem we are trying to solve by using these instruments. We call surface reconstruction problem, the task of retrieving useful quantitative corneal data from the raw information obtained by an imaging system. The problem is considered in the perspective of a videokeratoscope based on the Placido disk principle which is the case of our prototype. The formulation of the problem and its equations were present by Yobani and Daniel ().

Consider the simplified schema of Figure 2.4. To start any surface reconstruction,

first it is important to get samples from the image obtained with the reflection of the concentric rings. Consider the whole system to be in the same cartesian coordinates system where $(0, 0, 0)$ corresponds to the corneal apex and is aligned with the optical axis of the imaging system used. The samples are associated to the points on the edges of the reflected pattern, more precisely the samples are the positions of such points $S(S_x, S_y, S_z)$.

Let $Q(Q_x, Q_y, Q_z)$ be a point on the corneal surface, $P(P_x, P_y, P_z)$ be a point on the surface of the pattern cone and whose reflection was captured by the imaging system at position S . Consider the incident ray $\vec{u}(u_x, u_y, u_z)$ and the reflected ray $\vec{v}(v_x, v_y, v_z)$.

Let α be a scalar. We can represent Q as a combination of \vec{u} and P , as shown by the equations 2.1, 2.2 and 2.3.

$$Q_x = P_x + u_x\alpha \quad (2.1)$$

$$Q_y = P_y + u_y\alpha \quad (2.2)$$

$$Q_z = P_z + u_z\alpha \quad (2.3)$$

Let α' be another scalar. Hence it is also possible to derive Q from the combination \vec{v} and S as can be seen in Equations 2.4, 2.5 and 2.6.

$$Q_x = S_x - v_x\alpha' \quad (2.4)$$

$$Q_y = S_y - v_y\alpha' \quad (2.5)$$

$$Q_z = S_z - v_z\alpha' \quad (2.6)$$

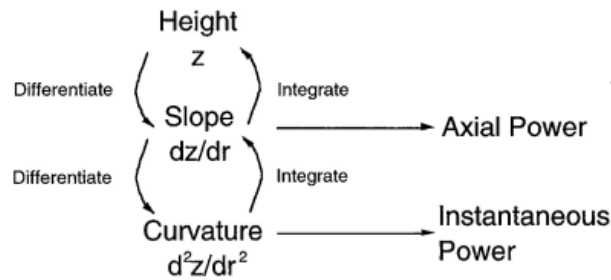
We can combine equations 2.1 and 2.4 to obtain the value of α as shown in the equation 2.7. The value of α' can be obtained through equations 2.2 and 2.5, resulting in the equation 2.8.

$$\alpha = \frac{v_y(S_x - P_x) - v_x(S_y - P_y)}{(u_x v_y - u_y v_x)} \quad (2.7)$$

$$\alpha' = \frac{u_y(S_x - P_x) - u_x(S_y - P_y)}{(u_x v_y - u_y v_x)} \quad (2.8)$$

By this results we can conclude that once we know the location of an image point S and its corresponding source point P , as well as the direction of the incident and reflected

Figure 2.5: Hierarchical ladder of corneal height, slope, and curvature, and the conversion between steps. Axial power is related to the slope data and the curvature of the cornea.



Source: Schwiegerling and Greivenkamp ()

rays, we will be able to precisely calculate the coordinates of the point Q on the corneal surface (YOBANI; DANIEL,).

Through this mathematical formulation proposed by Yobani and Daniel (), it is possible to determine the actual position of points on the surface of the cornea. Schwiegerling and Greivenkamp () defends that a corneal topographer should focus on obtaining such information, in particular the height (z coordinate), since it may be used to derive other kinds of useful data as stated in figure 2.5. Nevertheless, many surface reconstruction algorithms (KLEIN, b; HALSTEAD et al., ; KLEIN, c) will primarily obtain slope information which must be integrated in order to obtain the real three dimensional surface description.

One of the main limitations of this formulation is that supposedly it was possible to know the incident ray direction which is most likely not to be the case, since the source light used by regular Placido disk topographers is usually divergent. Also, obtaining the corresponding pair of points P and S is not a quite simple task due to tangential ambiguity. This is addressed by assuming both points to lie on the same plane as the point Q (MATTIOLI; TRIPOLI,), which is not always valid for surfaces with no rotational symmetry. To avoid these problems, some authors proposed modifications in the Placido disk pattern. Some proposed the insertion of radial lines (RAND; HOWLAND; APPELEGATE, ; BARSKY; KLEIN; GARCIA,), and Halstead et al. () proposed the use of a dartboard pattern.

Since an analytical solution for the reconstruction problem is unlikely, it is important to understand the limitations of the problem being considered. Nevertheless, strategies have been proposed to approximate a solution for it, each one of them normally relying on a different set of assumptions and conditions that may lead to slightly different results depending on the imaged data (e.g., Arc-Step algorithm (DOSS et al.,), Klein's

algorithm (KLEIN, b), Normal Fitting algorithm (HALSTEAD et al.,). Nevertheless, the algorithms used by commercial topographers are guard industrial secrets.

2.4.1 The Skew Ray Error

Most solutions for the surface reconstruction problem work on a per-meridian basis. Reconstructing one profile at a time, means solving the problem posed for every meridional plane individually. This means assuming that the optical axis, the surface normal, incident ray and reflected rays all lie on the same plane. For surfaces with rotational symmetry, this assumption is valid. Although for more general cases, specially corneas with astigmatism or that have undergone surgery, this assumption will possibly lead to errors, since some of the reflected rays tend not to stay on the meridional plane. These reflected rays are called *skew rays* and introduce an error most known as skew-ray error.

Although reconstruction algorithms have been proposed to handle the skew ray error (KLEIN, c), for the range of toricities seen in normal corneas, the skew ray error is considered to be negligible (HILMANTEL et al., ; KLEIN, a). Therefore reconstructing meridian by meridian is still considered accurate enough for daily clinical practice.

2.4.2 Corneal Topography Main Issues

As for the hardware, there are some fundamental limitations for data we can retrieve by means of a conventional Placido-disk-based corneal topographer. The main one is that the construction of a three dimensional surface from a two-dimensional image does not provide an unique computational solution. Therefore, only with assumptions of continuity and differentiability, and knowledge of the location of its apex can unique solutions to the slopes and locations of points on the surface be found (APPLEGATE R.; HOWLAND,). Also, as previously stated, it may not be valid for pathological or surgically modified corneas, which are normally the most important and interesting cases for clinicians and researchers.

Although much has been discussed about the uniqueness of a topography reconstruction using the reflection of the Placido disk, there are theoretical (e.g., artificially modeled) examples of corneas whose surface can not be reconstructed by using concentric circles patterns (RAND; HOWLAND; APPLEGATE,). These surfaces simply do

not contain any information in the tangential direction, only varying in the sagittal plane. Although, not very common, this may be caused by surgical procedures.

Corneal topographers aims to generate the same amount of samples for each ring. Nevertheless, accurate sampling of the inner rings are progressively more difficult. Since as one approaches the corneal apex, the number of pixels available gets lower and lower. Hence, depending on the topographer's imaging system resolution, not even sophisticated algorithms may be able to define accurately each sampling point. This becomes even a bigger issue since the center of the cornea is crucial to retinal image formation (APPLEGATE R.; HOWLAND,). Some topographers avoid this problem by taking magnified pictures.

2.5 Data Visualization

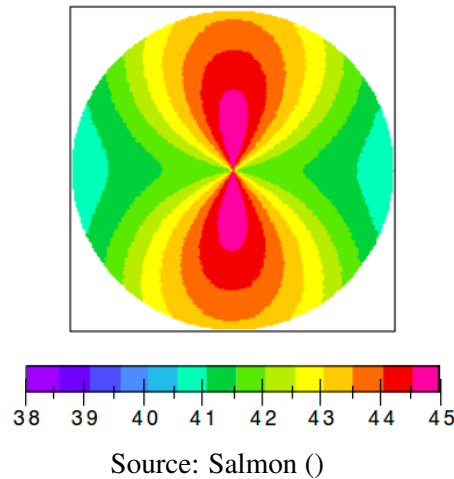
Solving the surface reconstruction problem produces a huge volume of data. Therefore, efficient methods are needed to extract high level information from it. Next, we will discuss the the main tool used for extracting high-level information from the captured data: color coded maps.

Color coded maps are one of the main tools for corneal topography data visualization because they convey a lot of information at a glimpse. They are the main solution adopted by most commercial topographers. Nevertheless, to provide information that is required by specific tasks, different kinds of color coded maps become available. We will briefly discuss the most used kind of color coded maps: *the axial curvature maps* (SALMON,).

The shape of the cornea is determinant for corneal optics (APPLEGATE R.; HOWLAND,). Therefore, it is quite natural to imagine these maps as color height maps. Nevertheless, this is often not the case. The corneal height variations of analytical interest tend to be two to three orders of magnitude smaller than the profile variations of a normal cornea's meridian. There is a dynamic-range problem in the display of the data (SCHWIEGERLING; GREIVENKAMP,). In order to solve this problem, instead of using directly the height values to generate the maps, it is subtracted a value relative to another surface. Thus, the maps usually display the deviations of the reconstructed surface with respect to a reference surface (e.g., spherical, aspheric, toroidal surfaces).

Clinicians, on the other hand, usually prefer to work with a more familiar kind of measurement. Hence, diopters are the measure usually used for color maps maps. It is

Figure 2.6: An example of axial curvature map.



important to clarify that, in this context, diopters may be used both to quantify a surface curvature or a surface refractive power, hence also being known as *dioptric curvature*.

By assuming the center of curvature to be on the optical axis, one can calculate the value of the axial radius of curvature (sometimes also referred as sagittal radius of curvature) as the distance from a given surface point S and the intersection of optical axis with a line along S's normal direction. This assumption is only valid for rotationally-symmetric surfaces, but since the region around the cornea apex tends to be more spherical, this assumption becomes reasonable. Therefore, axial radius of curvature is more precise around the central areas, introducing bigger errors in the periphery of aspheric surfaces (SALMON,). An example of axial curvature map may be seen in figure 2.6.

3 RELATED WORKS

This Chapter discusses a series of related works that consider the use of mobile technology, in particular the use of smartphones, to provide affordable visual acuity assessment. Demand for this kind of tool is arising specially in emerging and low-incoming countries.

We categorize the related works in two main categories. The first one contains works related with general visual acuity assessment, focused on visual low-order aberration assessment and preventive vision care. The second one contains works related to the creation of portable and low-cost corneal topographers. The second category is directly related to the subject of this thesis.

3.1 Visual Acuity Assessment

Many researchers have worked on designing low-cost solutions to address the visual acuity assessment problem. The majority of these technologies rely on a smartphone to provide, beyond portability, and precise measurements. We discuss three successful endeavors in this sub area.

First, Pamplona et al. (a) proposes an interactive method for estimating one's refractive condition. The assessment is done in close range by coupling a smartphone with a portable gadget (Figure 3.1).

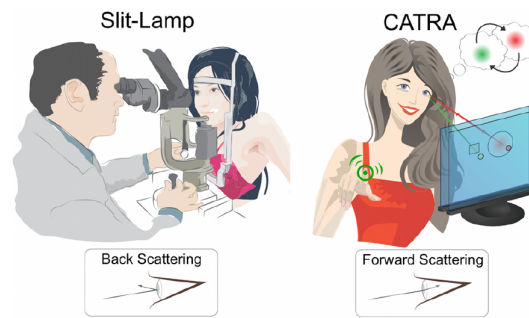
Cataracts is the leading cause of blindness worldwide. Available assessments for this condition usually demands expensive equipment and highly trained clinicians. More-

Figure 3.1: Schema represents the process of visual assessment using NETRA and the result on a smartphone screen.



Source: Pamplona et al. (a).

Figure 3.2: Cataract assessment using slit lamp on the left and CATRA on the right.



Source: Pamplona et al. (b).

Figure 3.3: Visual acuity assessment in small children using eye tracking.



Source: PEEK's website.

over, the standard examination approach based on the backscattering does not address the its detection during its early stages.

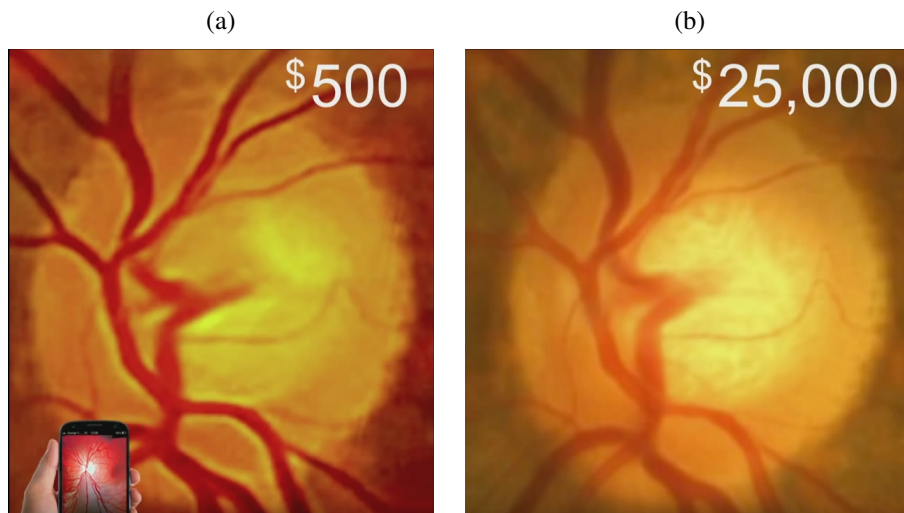
CATRA was build with the goal of providing inexpensive and easy way to perform cataract diagnostic. It also improves the reliability of the assessment process by taking into consideration the input from the subject being examined. This interaction improves early and mid stage cataract examinations. The CATRA approach can be seen in Figure 3.2.

PEEK, or Portable Eye Examination Kit, is a set of tools (both apps and gadgets) created by a series of researchers with the goal to empower local community health care workers in low-incomming countries¹. It allows, with minimum training, visual acuity assessment for people of all ages. An example of the tool, part of the PEEK project, to assess vision of infants can be seen in Figure 3.3.

PEEK uses the computational power of hand-held personal computers in performing several eye health-care examinations and diagnostics. For instance, in the case of retinal examination, a clipping gadget attached with magnifying lens allows for retinal examination with quality comparable to expensive industrial specific hardware devices (Fig-

¹<http://www.peakvision.org/> (Last visited 15/11/2015)

Figure 3.4: Comparison of retinal images obtained using PEEK (a) and a commercial device (b). The value of each system used being displayed on the right top corner of each image.



Source: PEEK's website.

ure 3.4).

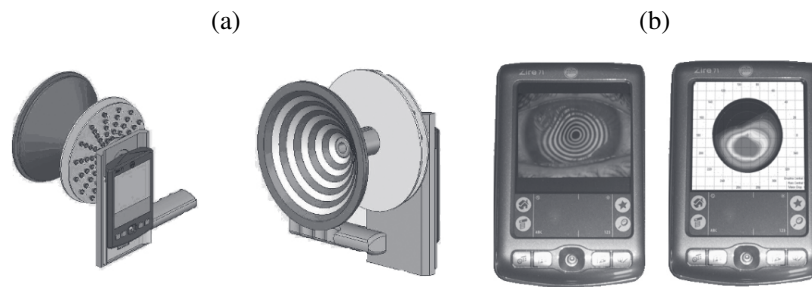
A backpack with solar panels attached to it allows the smartphone to stay charged and avoid energy supply problems, which are common in most rural and remote locations. The kit also can connect to a network to allow health organizations to locate those in need for surgical procedures and treatments, based on the measurements done by the examination kit.

3.2 Portable And Low-Cost Corneal Topography

Although eye's health care have technologically evolved in the past years, Placido-disk based corneal topographers are still the industry standard. The simplicity of its core principle has inspired the creation of several projects that aim into the creation of a portable, low-cost and affordable corneal topographer. We discuss three such initiatives: Carvalho (), Rosa () and Pinheiro et al. (). The last one was developed concurrently to this thesis.

Carvalho () created a corneal topographer that can be attached to a palmtop computer (design on Figure 3.5(a)). Due to restrictions by the time it was created, this solution was designed using limited computational power, besides capturing images on low resolution cameras. The reconstruction algorithm proposed by this work relies on calibration spheres. Its precision and simplicity (even in such restraining setup) convinced us to use

Figure 3.5: A corneal topographer for palm device (a) and the results obtained using it (b)



Source: modified from Carvalho ().

Figure 3.6: The corneal topographer prototype proposed by Rosa ().



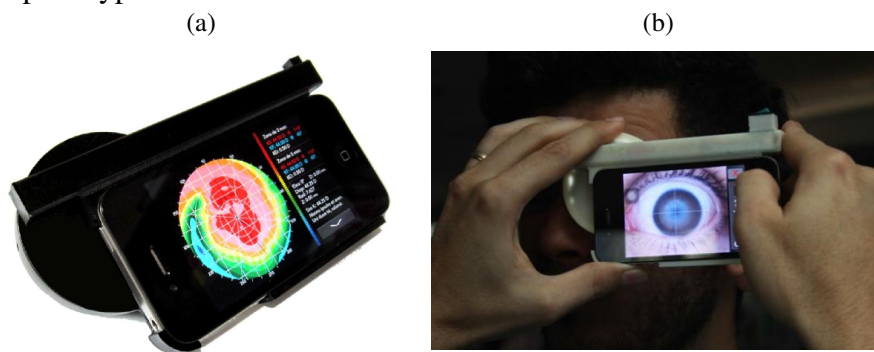
Source: Rosa ().

the same reconstruction algorithm in our prototype.

Rosa () proposed a smartphone-based corneal topographer. The designed gadget was made of acrylic panels while the light source consisted of a panel of LEDs connected to an external power supply. The work provided an image processing pipeline for dealing with the images acquired with the reflected Placido disk pattern. It used Klein's algorithm (KLEIN, b) for corneal surface reconstruction.

Pinheiro et al. () proposed a corneal topographer composed of a smartphone with a gadget attached to it. The gadget was printed using a 3D Dimension Elite Stratasys printer, suited for industrial quality production. They use stainless steel spheres of known radius in the process of calibrating the device. The lighting system is powered by batteries. Figure 3.7 shows the pictures of the prototype.

Figure 3.7: The corneal topographer developed by Pinheiro et al. (). (a) the prototype, and (b) the prototype in action.



Source: Pinheiro et al. ().

4 A LOW-COST CORNEAL-TOPOGRAPHY APPROACH

In this chapter we introduce our road map for building a low-cost corneal topographer. We present a pipeline our ideas towards a low-cost and efficient design. We empower those ideas with a series of flexible software solutions that can be used to simulate all the stages of the pipeline.

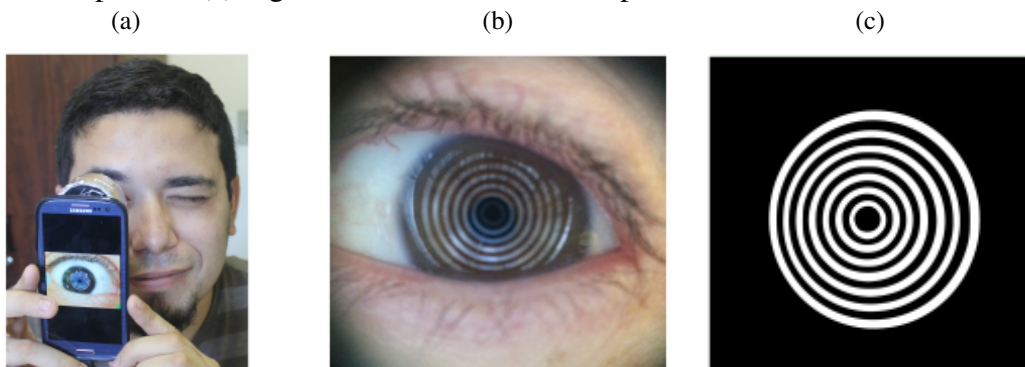
We start by presenting the stages of our topographer's pipeline. Then, we introduce our software based strategies used to explore our topographer's design. Then, we discuss the process of setting up our reconstruction algorithm through calibration. Finally, the reconstructed data is used to generate some high-level information, such as color maps.

4.1 Corneal Topography Pipeline

Our pipeline is basically divided into three main interlinked stages which are executed serially. We now detail each one of these stages.

The first stage, it is the **Image Acquisition**. This stage address the process of imaging the subject's corneal surface. We have chosen the approach in which the subject's cornea has to be imaged while reflecting a pattern of concentric rings, this pattern is known as Placido disk (Chapter 2). Although we could have used different patterns such as the one proposed by Rand, Howland and Applegate (), it has been already shown that traditional Placido disk pattern yields satisfying results, besides its simplicity and easy of creation (KLEIN, c). Figure 4.1 exemplifies the image-acquisition stage. It is necessary

Figure 4.1: Details of the main steps during the process of image acquisition. (a) the imaging process for a subject's corneal surface, (b) captured image exhibiting the reflected Placido disk pattern, (c) segmentation of the reflected pattern.



Source: the authors.

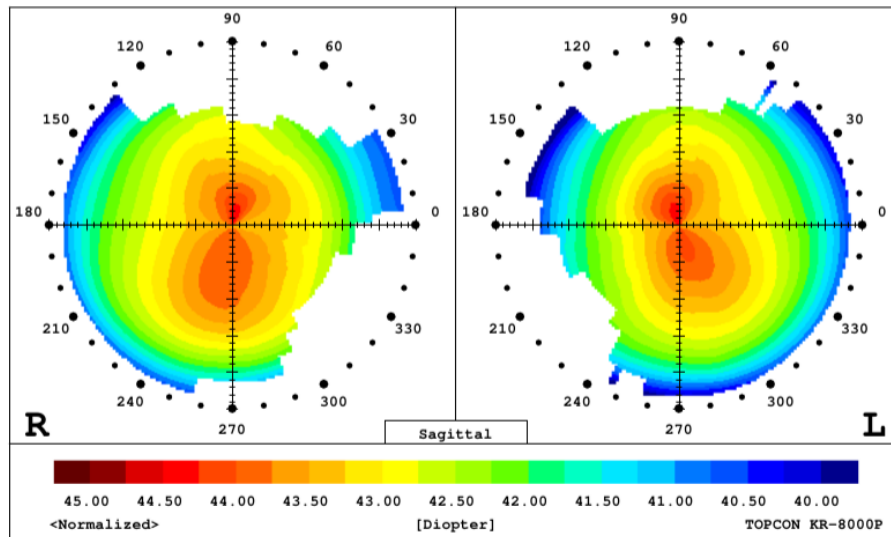
to build a device that will be attached to the smartphone. It will hold pattern and help to correctly position the subject's eye with respect to camera-pattern system. Given a captured image containing the reflected pattern (Figure 4.1(b)), we need to segment the image in order to extract the useful data from it, to achieve a result similar to the one in Figure 4.1(c).

The second stage is responsible for the **Surface Reconstruction**. At this point, the topographer uses all the information gathered from the previous stage to create a physical description of the subject's cornea. The term *reconstruction* might induce one to think it actually creates a three dimensional representation of the surface, but here it refers to the reconstruction of curvature data. APPELATE R.; HOWLAND (), Yobani and Daniel () discuss the theoretical and practical limitations when using Placido-based topographers to build a three dimensional representation. Thus, a Placido-based system usually yields a description of curvature for the surface at many different points. It is important to notice that this information could be integrated to achieve a three dimensional representation (SCHWIEGERLING; GREIVENKAMP,). However, such a 3-D reconstruction lacks clinical reliability since this is an ill-posed problem (KLEIN, a). Also, the description of curvature is often considered to be the most valuable information provided by a corneal topographer to daily clinical practice.

This stage is probably the one that has been more researched by the community. There are plenty of different techniques to built such curvature data. Later, we discuss in more detail how our topographer reconstructs corneal curvature. All the information gathered from this stage is used as input for the third and last one.

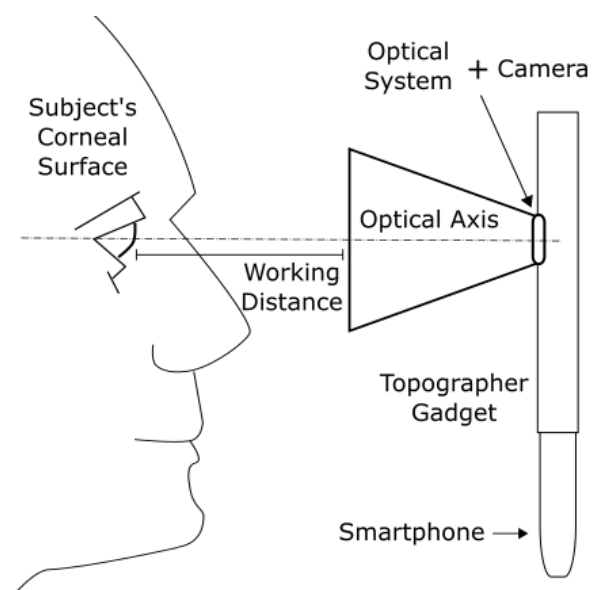
The third stage is the **High-Level Data Extraction**. The reconstruction data is used to create Axial Power Curvature color maps, which are the default output provided by a corneal topographers (even non-Placido-based systems). By grouping the information into meridians, we can provide a simulated keratometry. It consists of identifying main keratometric curvatures and its corresponding axis. With this information, we can also evaluate the subject's corneal degree of astigmatism. Figure 4.2 shows an Axial Curvature color maps produced by the commercial corneal topographer Topcon KR-8000PA¹.

Figure 4.2: Axial curvature color map obtained by the reconstruction of both eyes of a subject. Missing information probably caused by the nose occlusion and the noise interferency from the palpebras.



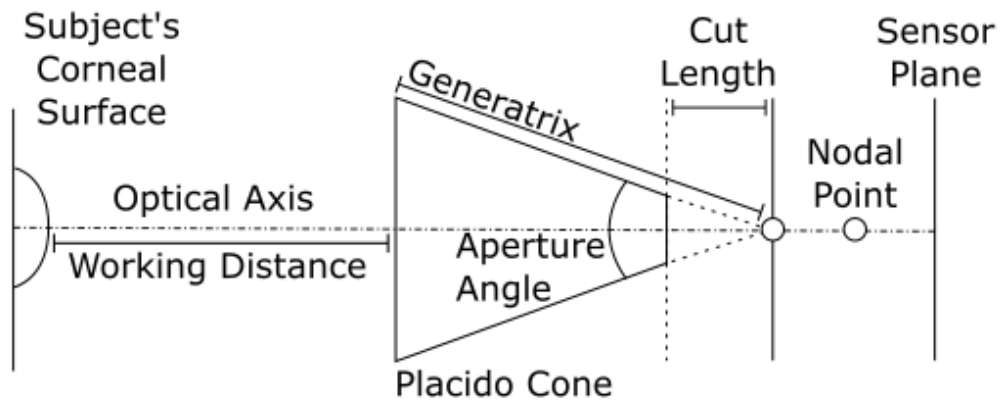
Source: image generated by Topcon KR-8000PA's proprietary software.

Figure 4.3: A scheme which portrays all the main elements of our intended topographer design.



Source: the authors.

Figure 4.4: This simplification exposes the core features of our previous design.



Source: the authors.

4.1.1 Corneal Topographer Design

Figure 4.3 shows a schematic representation that summarizes our Placido-based system design. It consists of a Placido cone, attached to smartphone, whose camera observes the reflected pattern through a hole in the cone. Notice that this simplification is mostly inspired by the traditional Placido Disk tool (PLÁCIDO,).

Physical features of the topographer device have huge implications in the final topographer's performance. For instance, they define its maximum area of coverage, number of circles in the reflection (which limits the data being retrieved and the sampling points), and impacts the precision of the topographer's results. While such features are crucial for any design, to the best of our knowledge, no discussion on the impact of these elements is available in the literature.

The core features of our design are summarized in Figure 4.4. They are the *Placido cone*, hereby defined by its aperture angle (which can be up to 180°), its *generatrix* and the distance from its vertex where it should be truncated (*cut length*). The *nodal point* simplifies the optical system being used. The sensor plane which represents the camera sensor. Finally, the *working distance* of the system is defined as the distance between the base of the cone and the corneal surface apex. The cone is truncated near its vertex so the camera can image through it. The cone's internal surface holds the Placido disk pattern to be reflected on the subject's corneal surface.

¹<http://www.topconmedical.com/> (Last visited 11/05/2015)

4.2 The Corneal Topography Simulation

Since the output of one stage of the pipeline is directly used as the input of the next one, errors tend to propagate from one stage to another. Therefore, its implementation requires a very controlled environment if we want to study and validate it. It is very important to consider the implications of noisy inputs. As one can imagine, the first stage is the most vulnerable to noise. Camera or subject motion during image acquisition, misalignment when positioning the topographer in front of the subject's eye, and gadget mispositioned while attached to the smartphone are only a few of the possible issues that can severely interfere on the topography data obtained. These issues are very difficult to detect and repair (ALKHALDI et al., ; ALKHALDI, ; CANEIRO; ISKANDER; COLLINS,). To study the impact of these and other issues in a controlled environment, we have created a software environment where we can simulate all relevant aspects involved in a corneal topography setup. We have used this environment, to evaluate and validate our topography pipeline.

Following, we present approaches to simulate a corneal surface and its imaging process. As the simulation is free of most possible sources of noise, it allows us to obtain reliable data to feed next stages. Hence, it allows us to partially validate our topographer. We present details about the creation of this environment.

4.2.1 Modeling the Corneal Surface

The surface of a normal cornea is known to be slightly oval when viewed frontally, it is similar to a rotationally symmetric ellipsoid. It has a radius that varies less towards the central region and varies more towards the limbus (HELMHOLTZ,).

There are many approaches that can be used to model the cornea surface. The simplest one would be to use polynomial or parametric curves. It can take advantage of the cornea's rotational symmetry, reducing the problem to a simple profile description. Using simple Raytracing techniques, it is possible to obtain an analytical solution. This approach was indeed the first one we experimented with, more specifically, we used Bézier curves to approximate the surface.

The problem of using a single profile curve is that when simulating low-order aberrations, such as astigmatism, it will require a cumbersome and less-intuitive interpolation between the meridians. This kind of deviation has an overall impact on the corneal shape

and more than a single profile is necessary to simulate it.

We then switched to a three dimensional representation that could more straightforwardly handle our intended software simulation. The problem of creating a mathematical model for the cornea has been previously addressed by some authors. Mandell and Helen () proposed a model where both principal meridians are perpendicular and modelled by ellipses. ??) proposed the cornea to be represented as an ellipsotric surface which is obtained by uniformly compressing the ellipsoid radius along a toric surface. We have chosen to use the ellipsotric surface model, since it provides enough information for us to control the overall corneal shape simply by defining its main radii and a shape factor. Although simple, these properties are able to represent the most common cases of aberrations required by our simulation.

An ellipsotric model consists of a height function defined in cylindrical coordinates. Let r_h and r_v to be the main radii for a simulated corneal surface. C will be the shape factor which represents the uniform compression along the toric surface. ρ is the radial distance from the rotational symmetry axis of the surface. And θ specifies the angle of the meridian being considered. Equation (4.1) express the maximum radius of a given meridian θ (SALMON, ; CHURMS,). The height of the surface at a given point (ρ, θ) is them represented by the function S expressed in Equation (4.2).

$$R(\theta) = \left[\frac{1}{r_h} \cos(\theta)^2 + \frac{1}{r_v} \sin(\theta)^2 \right]^{-1} \quad (4.1)$$

$$S(\rho, \theta) = \frac{r(\theta) - \sqrt{r(\theta)^2 - C\rho}}{C} \quad (4.2)$$

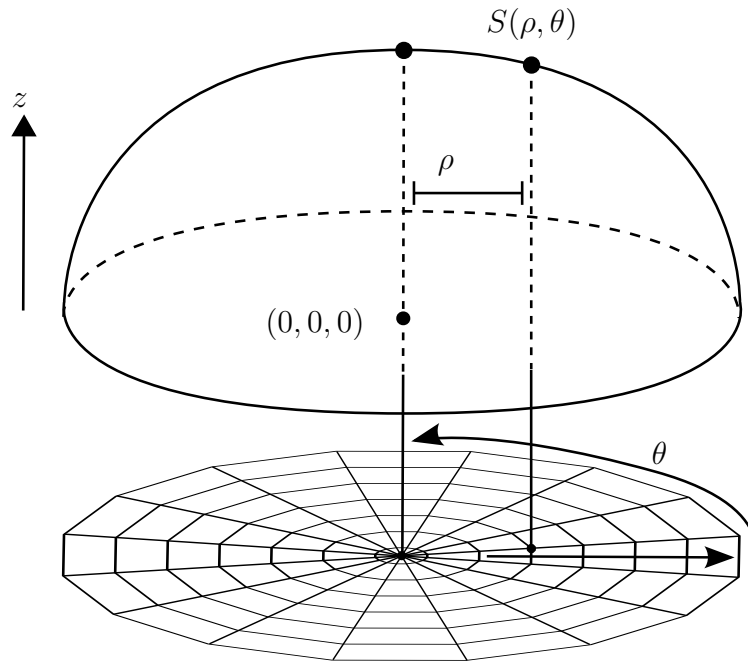
Using the model, it is possible to express a cornea with 2.81 D astigmatism simply by setting $r_h = 8.00mm$, $r_v = 7.50mm$, and $C = 0.85$, this case was described in Salmon ().

Figure 4.5 shows how our software samples the S function. The same coordinate system is used when simulating the topographer. Figure 4.6 shows a screenshot of our corneal-surface simulation system.

4.2.2 Simulating a Topographer System

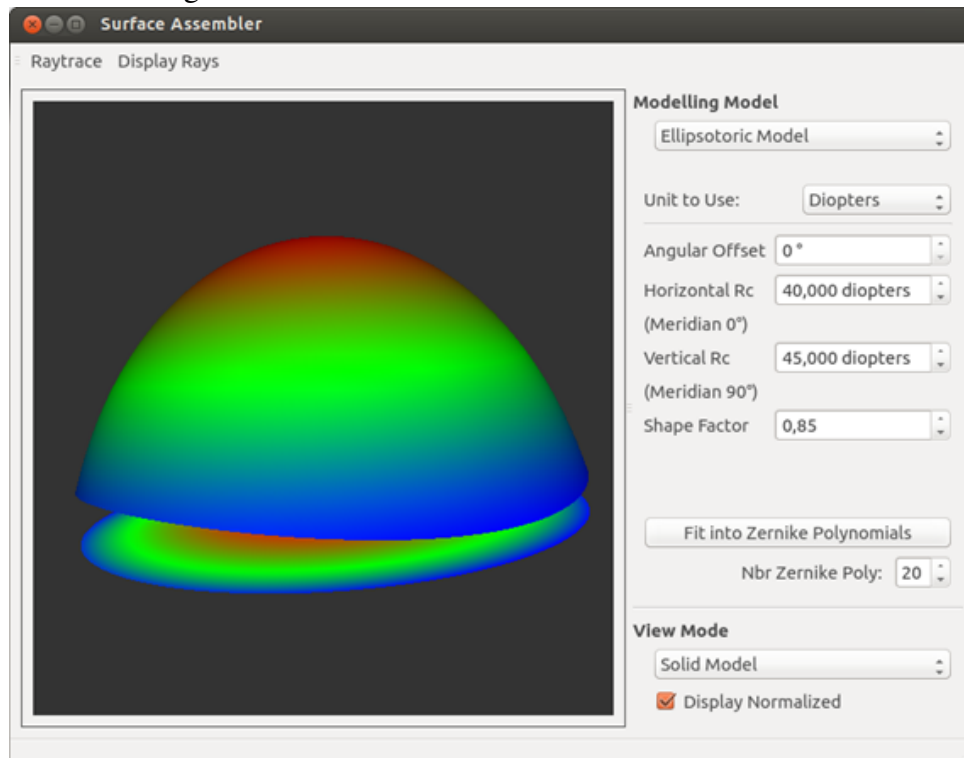
Besides simulating the corneal surface, we also simulate the projection of the Placido-disk pattern on the corneal surface. The projection apparatus can be simply rep-

Figure 4.5: The ellipsotoric model in cylindrical coordinates with the discretization approach we used in our software.



Source: the authors.

Figure 4.6: Our corneal surface simulation software.



Source: the authors.

resented by a truncated circular cone whose axis of revolution is aligned with the corneal rotational symmetry axis. The pattern to be reflected lies in its internal surface. A more detailed discussion about the pattern itself can be found in a further section. For most corneal topographers, the projection relies on the use of a source light positioned behind the projection apparatus. In commercial solutions sometimes a non-visible light (e.g., infrared) is used in order to ease the subject's experience, specially important for those with particular photosensitive conditions. But in our case, what we need is simply a function that once the apparatus's geometry have been set, we can calculate the color for any chosen point of its internal surface.

Together with the projection apparatus, we put in place a nodal point and a sensor plane with dimensions based on real smartphones CCDs. Particularly, we used the specifications of Samsung Galaxy S3TM obtained through the non-official site Sensor Size².

The projection apparatus, nodal point, and the sensor plane together with a predefined working distance, form our simulated topographer system.

4.3 Imaging the Simulated Cornea

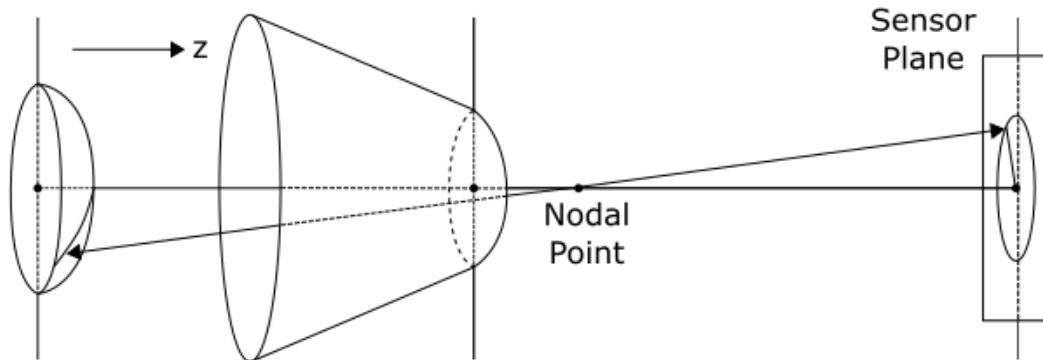
The next step is to effectively simulate the first stage of our topography pipeline by sampling data from our simulated corneal surface and then render these data as an image of the reflected. This process is performed following the conventional approach for raytracing. For each pixel of the output image, our system traces rays that originate at the center of projection of a virtual camera and go through a projection plane, finally reaching our three dimensional environment.

In our simulation, the camera's center of projection is at our nodal point, the projection plane is our sensor plane and the three dimensional environment is the simulated topographer system and the simulated corneal surface. The simulated cornea behaves as a perfect convex mirror and therefore reflects the environment. Hence, the resulting rendering is the reflected pattern on the cornea. The amount of pixels used and the quantity of rays per pixel are adjustable.

This rendering process yields a binary image. Following, we discuss two approaches to address the sampling for the raytracing algorithm: the *radial sampling* and the *general sampling*.

²<http://cameraimagesensor.com/> (Last visited 11/05/2015)

Figure 4.7: Relation between the meridians on the cornea surface and on the sensor plane. The double arrow demonstrates a match between a meridian from the surface and one meridian on the sensor plane. This relation is used in order to obtain an image directly into polar coordinates.



Source: the authors.

4.3.1 Radial Sampling

Radial Sampling is the fastest approach we achieved for this stage. It heavily relies on the rotational symmetry of our topographer system to provide fast and accurate solution for the raytracing. The approach consists in raytracing one meridian at the time, thus reducing our three dimensional problem to the two dimensional domain.

Lets consider that both corneal surface and the topographer system are perfectly aligned. A direct implication of this assumption is that we can obtain a direct relation between the pattern source and the meridians of the surface.

Since the *skew ray error* (Chapter 2) has negligible effect for the range of toricities seen in normal corneas (HILMANTEL et al., ; KLEIN, a), it can be ignored in our simulation. For each traced ray from the sensor plane, there is a meridian match on the surface. Figure 4.7 illustrates the match. This relation implies that for each traced ray, the surface can be represented by a function that describes the geometrical profile of a specific meridian.

Next, we present the analytical raytracing solution when using a Bézier curve to represent the surface profile. We choose quadratic Bézier curves due to their simplicity. Note that following procedures could easily be adapted to other types of curves.

Consider a ray T_i expressed by Equation (4.3), where O_i is the origin of the ray on the sensor plane, D_i is the direction from O_i to the nodal point. Our profile function f_p is expressed by a quadratic Bezier curve defined as Equation (4.4), where P_0 , P_1 and

P_2 are its control points, which are coplanar. These points are described in cylindrical coordinates. The first step of the raytracing solution is finding the intersection between the ray and the profile. This can be obtained analytically by solving the linear system represented by Equation (4.5).

$$T_i(\alpha) = O_i + D_i\alpha, \alpha \in [-\infty; \infty] \quad (4.3)$$

$$f_p(\beta) = (1 - \beta)^2 P_0 + 2\beta(1 - \beta)P_1 + \beta^2 P_2, \beta \in [0; 1] \quad (4.4)$$

$$f_p(\beta) - T_i(\alpha) = 0 \quad (4.5)$$

The normal vector of the profile at the intersection point is calculated using Equation (4.6) and Equation (4.7), where (m, n) is a vector tangent to the surface profile at the point $f_p(\beta)$. Using the direction of the normal N_i and of the incident ray U_i , a reflected ray V_i is calculated as in Equation (4.8). The direction of the reflected ray V_i is used to trace a ray from the intersection point towards the projection apparatus. Since we are dealing only with a two dimensional domain, this last intersection can be calculated by a simple line-to-line intersection.

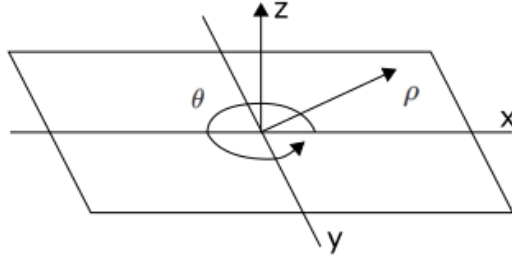
$$\frac{df_p(\beta)}{d\beta} = (m, n) \quad (4.6)$$

$$N_i(\beta) = (-n, m) \quad (4.7)$$

$$V_i = U_i - 2(U_i \cdot N_i)N_i \quad (4.8)$$

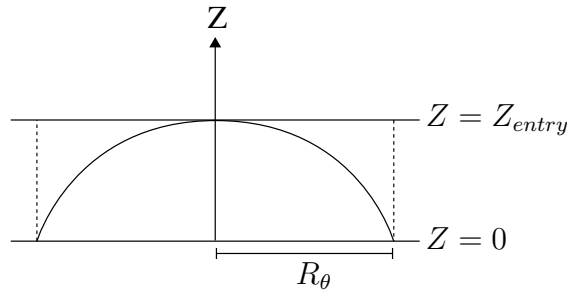
Solving the raytracing for the ellipsotoric surface is done in a similar fashion. Be f_θ the profile function describing the meridian θ of this surface model. Differently from the Bezier case, a closed analytical solution was not found. Fortunately, f_θ is a monotonic function, which allows us to solve the intersection through an iterative numerical approximation. To perform this search, the function $T_i(\alpha)$ will be rewritten in cylindrical coordinates. Since we are dealing with a three dimensional scenario, to avoid any confusion, we present a diagram of equivalence between the Cartesian coordinates and the cylindrical coordinates being used in Figure 4.8. It is important to note that the ray is expressed in a Cartesian coordinates system. We arranged our simulation so the Z axis coincides on the same axis in both coordinates system. For the two dimensional case we also have that $\rho = |x|$.

Figure 4.8: Equivalences between the Cartesian and cylindrical coordinates. The Cartesian system being expressed by (x,y,z) and the cylindrical one by (ρ, θ, z) .



Source: the authors.

Figure 4.9: The ellipsotric model in cylindrical coordinates with the discretization approach we used in our software.



Source: the authors.

Let $T_i(\alpha)_j$ be the scalar component j of the ray T_i for a given α value. The ray $T_i(\alpha)$ will then be expressed as $T_{i,cyl}(\rho)$, with $\rho \in [\rho_{apex}; R_\theta]$, where ρ_{apex} is the value obtained by Equation (4.9) and it is the ρ equivalent to the value of α where the ray T_i hits the ellipsotric surface bounding rectangle, which means that $T_i(\rho_{apex})_z = Z_{entry}$ (Figure 4.9); R_θ is the maximum radius ρ value for a given meridian θ . Note that S_{max} is the maximum height value obtained in the surface S . The ray form expressed in cylindrical coordinates is in Equation (4.10). It is important to notice that this form is possible since when $T_{i,z} < S_{max}$, necessarily $x = \rho$.

$$\rho_{apex} = \left| T_i \left(\frac{S_{max} - O_{i,z}}{D_{i,z}} \right)_x \right|, D_{i,z} \neq 0 \quad (4.9)$$

$$T_{i,cyl}(\rho) = T_i \left(\frac{\rho - O_{i,x}}{D_{i,x}} \right) \quad (4.10)$$

Consider Equation (4.11) with $\rho \in [0; R_\theta]$. Finally the solution of intersection I_r is the value of ρ which solves Equation (4.12).

$$f_p(\rho) = f_\theta(\rho) = S(\rho, \theta) \quad (4.11)$$

$$I_r(\rho) = f_\theta(\rho) - T_{i,cyl}(\rho) = 0 \quad (4.12)$$

A binary search is performed by assuming the monotonicity of the intersection Equation (4.12). The initial guess being as expressed in Equation (4.13). The existence of a solution is verified by the expression $I_r(\rho_{apex})I_r(R_\theta) < 0$.

$$\rho_0 = \frac{(\rho_{apex} + R_\theta)}{2} \quad (4.13)$$

Once and if the intersection point is found, the normal is computed by means of the Equation (4.14), which is numerically approximated. Note that $S(\rho, \theta)$ is defined in Equation (4.2).

$$S_{normal}(\rho, \theta) = \frac{\partial S(\rho, \theta)}{\partial \rho} \times \frac{\partial S(\rho, \theta)}{\partial \theta} \quad (4.14)$$

Similarly as before, using the S_{normal} and the incident ray direction, it is simple to calculate the reflected ray V_i by using the Equation (4.8). The last step is analogous to solving the raytracing for the Bezier curve and consists of the intersection between the reflected ray and the projection apparatus.

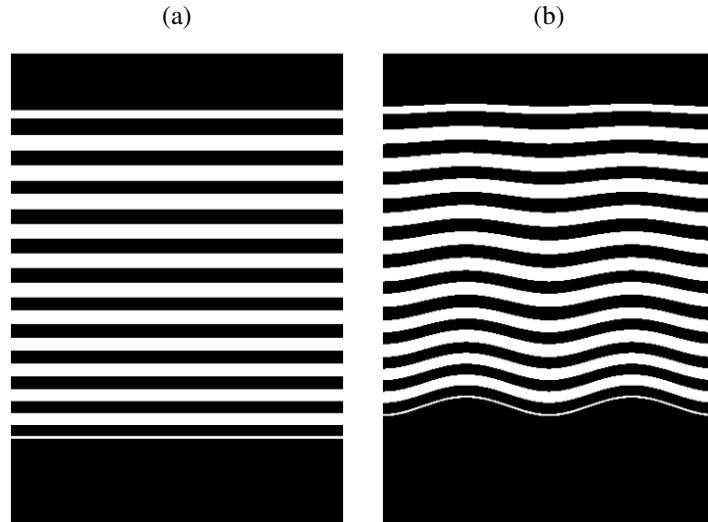
To assemble our result image, a ray is traced for each pixel of the sensor plane. In the cases where exists an intersection between the reflected ray and the projection apparatus, the color of the corresponding pixel will be the same as the one of the pattern at the intersection point. Whenever the ray does not intersect with the apparatus, the corresponding pixel's color is left black.

We have chosen to trace the rays a meridian at the time and accumulate columns of resulting pixels side by side. This way we can generate an image in polar coordinates, which prevents us from needing to calculate it later. Figure 4.10 represents a result obtained through the application of the *radial sampling*.

4.3.2 General Sampling

Radial sampling would be the plausible choice for our pipeline and simulation. However, it heavily relies on the alignment of the system with the subject, a situation hard to enforce in practice. To be able to handle scenarios where the topographer may be dislocated (translational or rotational) in relation to the surface, we propose the *general*

Figure 4.10: Radial sampling for two different surfaces. (a) there is the result for $r_h = r_v = 8.8mm$ and a shape $C = 1$, which is a subject with no astigmatism and perfectly spherical corneal surface; (b) the values $r_h = 8.00mm$, $r_v = 7.50mm$, and $C = 0.85$ were used, in this case simulating a subject with around $2.82D$ of astigmatism.



Source: the authors.

sampling. Affinne transformations can be applied to the whole topographer system, while preserving the components relative distances. The traced rays follow the same process as described on the previous sampling method.

The main difference in this process is the intersection between ray and the corneal surface. In this scenario, we need to calculate the intersection of the function $T_i(\alpha)$ with $\alpha \in [-\infty; \infty]$ and the function $S(\rho, \theta)$. For simplicity, the surface model is centered at the origin of the cylindrical coordinates.

The first step is writing the function T_i in cylindrical coordinates. The new functions are presented by Equations 4.15, 4.16 and 4.17.

$$\rho(\alpha) = \sqrt{T_i(\alpha)_x^2 + T_i(\alpha)_y^2} \quad (4.15)$$

$$\theta(\alpha) = \text{atan2}(-T_i(\alpha)_y, T_i(\alpha)_x) \quad (4.16)$$

$$z(\alpha) = T_i(\alpha)_z \quad (4.17)$$

The function $z(\alpha)$ is used to find the domain of possible solutions. Therefore, the α that intersects the surface must be in the range $[\alpha_{bot}; \alpha_{apex}]$. Values α_{bot} and α_{apex} represents the intersection between the ray and the surface bounding box sides which are perpendicular to the z axis (Figure 4.9). Their values are obtained from Equations 4.18 and 4.19.

$$\alpha_{bot} = -\frac{O_{i,z}}{D_{i,z}} \quad (4.18)$$

$$\alpha_{apex} = \frac{S_{max} - O_{i,z}}{D_{i,z}} \quad (4.19)$$

Once again the solution for the intersection is the root of the function I_g , now more easily represented in terms of α , as can be seen in Equation (4.20) .

$$I_g(\alpha) = z(\alpha) - S(\rho(\alpha), \theta(\alpha)) = 0 \quad (4.20)$$

The function I_g in Equation (4.20) is not necessarily monotonic, what makes the previous search strategy unfeasible. It happens because any direction and alignment might be in place. The intersection can be found by performing an iterative linear search. This search is done using the following algorithm in pseudo-code.

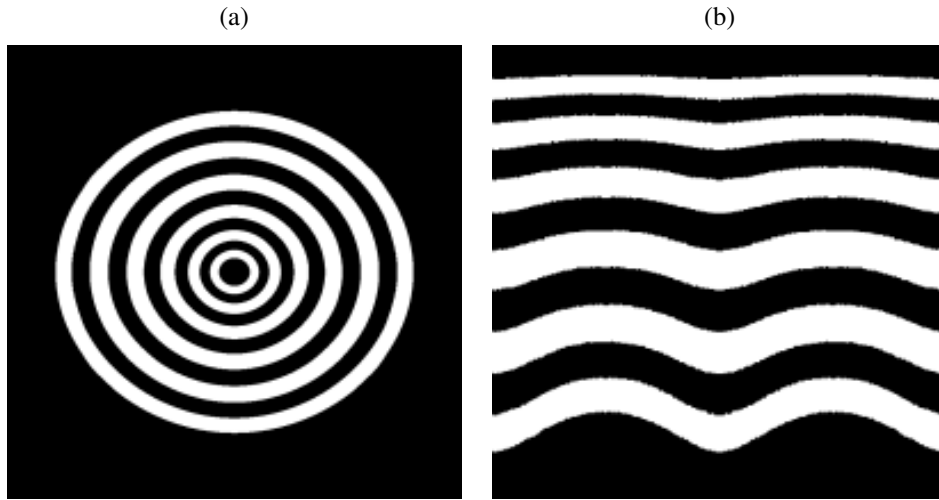
1. Define a possible range of α values for the solution $[a; b]$.
2. Subdivide the interval $[a; b]$ in N equidistant points $[k_1, k_2, \dots, k_n]$, where $k_1 = a$ and $k_n = b$.
3. Search for an interval $[k_j, k_{j+1}]$, such that $I_g(k_j)I_g(k_{j+1}) \leq 0$. Meaning there is a solution in this range.
4. If step 3 found a possible interval, then set $a = k_i$ and $b = k_{i+1}$, otherwise increase N .
5. if $I_g((a + b)/2)$ is inside an error tolerance, the intersection has been found. Otherwise consider the value of N . Is it big enough? If yes, then assume there is no intersection, otherwise continue.
6. go to step 1

Clearly, the performance of the *general sampling* is slower due to this iterative search. Also ideal values for N and error tolerated were chosen empirically. As a side effect, alias artifacts are generated in the final image.

Once the intersection of the ray with the surface is computed, the other steps of the raytracing process remain analogous. However, differently from *radial sampling*, this one is done in a scan line fashion. The final image is generated a line at the time which does not provide an image already in polar coordinates.

An example of resulting image from General Sampling can be seen in Figure 4.11(a). It must be converted to polar coordinates, as can be seen in Figure 4.11(b), before being

Figure 4.11: In the image we have the result of the general sampling for a surface with $r_h = 8.4mm$ and $r_v = 7.5mm$. In (a) the resulting raytraced image and in (b) the result of the conversion to polar coordinates.



Source: the authors.

used by next pipeline stages.

The process to convert the raytraced image to a polar coordinates representation is straightforward and only requires to resample the image through a mapping function. Consider $Img(r, \theta)$ to be the desired final image in polar coordinates, and $Crt(x, y)$ to be the result of our raytracing process. The mapping can be expressed in Equation (4.21). Due to angular discretization, there will be oversampling of more central regions. Also there will be loss of information between consecutive sampled meridians at the peripheral regions. Although the same happens when performing the *radial sampling* approach, it does not calculate any ray information that is lost when creating the final image.

$$Img(r, \theta) = Crt((1 + \cos(\theta))r, (1 - \sin(\theta))r) \quad (4.21)$$

4.4 Crafting a Corneal Pattern Through Simulation

A core element of the design of our topographer system is the Placido disk pattern. In the imaging process, it appears attached to the inner side of the truncated cone, projection apparatus. The pattern itself consists of a series of concentric circles usually alternating between black and white. Commercial solutions also use others color schemes, such as the Chroma by Wavetek³ (Figure 4.12).

A planar projection apparatus can be found in some commercial corneal topogra-

³<http://www.wavetek.com.br/wavetek/chroma-analisador-de-cornea> (Last Visited 11/05/2015)

Figure 4.12: Corneal Topographer Chroma by Wavetek. Notice it uses a pattern with red, green, blue and black colors.



Source: Wavetek's website.

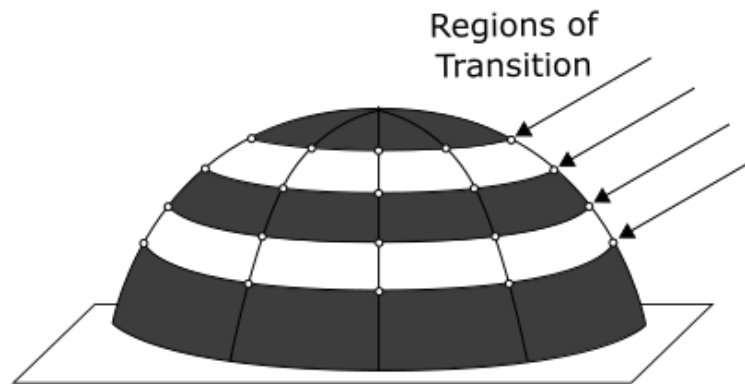
pher such as Topcon KR-8000PA. This geometry requires the pattern to have a considerable size in order to cover enough of the corneal surface, while restraining the possible working distances of the device. They also tend to have more problems with occluded areas, specially at zones near to the subject's nose.

The hemisphere design is capable of covering a wider area of the cornea, minimizing the interference of corneal regions being occluded (KNOLL; STIMSON; WEEKS,). Some authors justified the use of a truncated cone shape instead of a hemisphere shape since it has easier manufacturing without compromising the topographer accuracy (YOBANI; DANIEL,). The truncated cone is our design choice due to its simplicity and accuracy.

The main difficulties to the creation of a pattern for a topographer are: the number of circles to be used, the thickness of each circle, the dimensions of the truncated cone shape or the use of a planar shape for the projection apparatus. We have not found enough information on those topics. Hence, we decided to investigate some of them using our simulator.

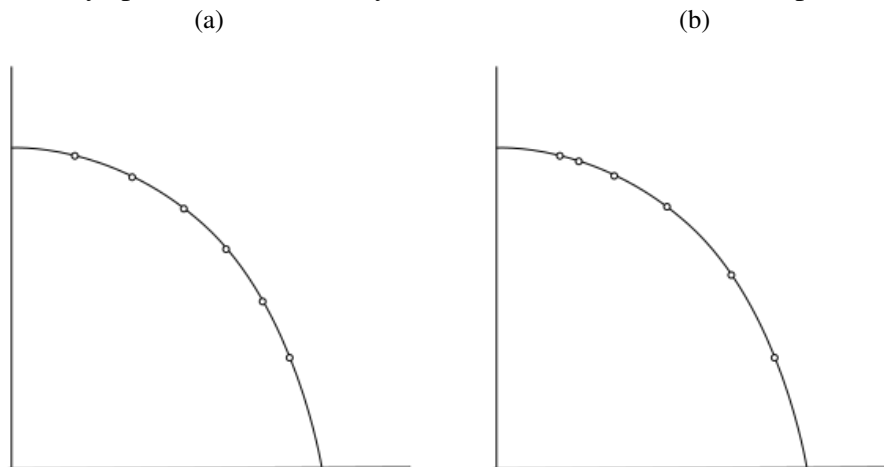
Further discussion about the physical creation of the projection apparatus and some of the effects from its properties can be found in the next chapter. Following, we explore a strategy for the pattern creation once the projection apparatus shape has been set.

Figure 4.13: A surface reflecting the Placido disk pattern. Note the regions of transition and the arcs defined over the surface. The dots on the surface are examples of positions where we actually extract data.



Source: the authors.

Figure 4.14: Two regions of transition distribution over the same profile. In (a) the sample points are evenly spaced and in (b) they are concentrated towards the top.



Source: the authors.

4.4.1 Pattern Creation using Inverse Sampling

Topography data is reconstructed only on the regions of the pattern corresponding to transitions between concentric circles of different colors (see Figure 4.13). Given a typical eye shape, it is very likely that the reflection of the pattern will be distorted, so there will be an uneven distribution of regions of transition, meaning the arcs formed between consecutive regions are likely to have different lengths (see Figure 4.14).

We propose a process for creating a pattern of concentric circles whose reflection on a predefined surface can be controlled. Hence, one can create a pattern where the regions of transition are positioned on a set of chosen locations. In particular, we used

this technique to calculate a regular pattern, whose regions of transition are evenly distributed (see Figure 4.14(a)). Thus, the data is reconstructed at a regular rate throughout the surface. It is important to note that this procedure can be used in many different ways. For instance, one may want to have more regions of transition towards the central portion of the intended surface, similarly to Figure 4.14(b).

Also, keep in mind that for corneal assessment not only absolute reconstruction values are important. It is very useful to understand the deviation of one subject from a predefined geometry (SCHWIEGERLING; GREIVENKAMP,). Therefore, one of the advantages of using a regular pattern is that more information can be obtained simply by comparing the result of the imaging process of a subject and the imaging of the reference surface. Note that the regular pattern is computed for a specific projection apparatus shape and working distance.

The regular pattern is created by a process of raytracing similar to the one described for the *radial sampling*. It is important to consider that regardless the surface model used, we will deal with the problem of handling a single meridian at a time. So the only restriction imposed is that the used model can be represented as a set of functions describing meridian profiles.

Consider a standard surface defined by the function $S(\rho, \theta)$. Be $S_i(\rho) = S(\rho, \theta_i)$, where θ_i is a predefined meridian. Hence, S_i is the function that describes the profile of the surface at the meridian θ_i . We will define an arc of the profile to be a pair (ρ_i, ρ_{i+1}) , where $\rho_{i+1} > \rho_i$ and they are the arc's extremities.

Our strategy consists of calculating a set of arcs whose extremities are located exactly where we intend to place the pattern's regions of transition. Afterwards, we use the law of reflection to calculate where on the projection apparatus this transition needs to be. We call this process *inverse sampling*.

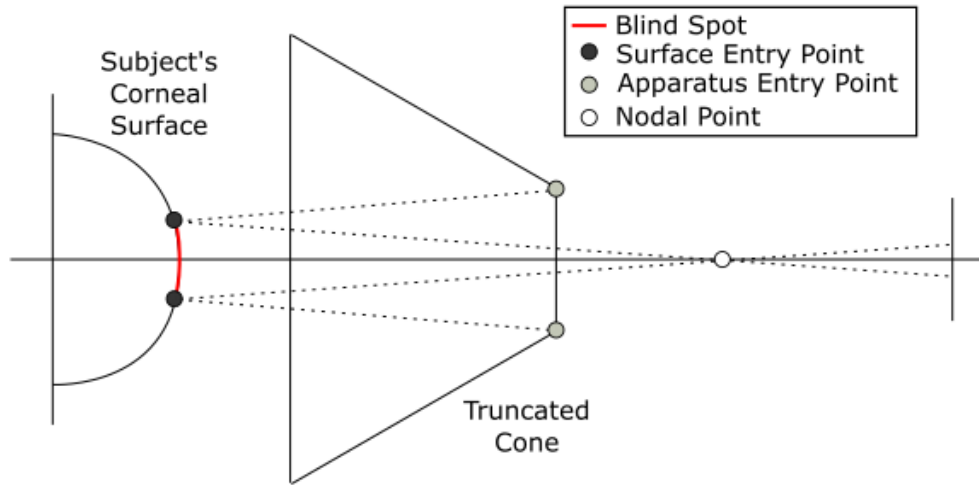
4.4.1.1 Calculating the Arcs

Let L_i be the length of the arc (ρ_i, ρ_{i+1}) defined as the Equation (4.22). The total length of the meridian profile L_i^{max} is therefore the length of an arc $(0, \rho_i^{max})$.

$$L_i(\rho_i, \rho_{i+1}) = \int_{\rho_i}^{\rho_{i+1}} \left| \frac{dS_i(\rho)}{d\rho} \right| d\rho \quad (4.22)$$

As presented in Guenter and Parent (), Equation (4.22) can be solved by means of an Adaptive Gaussian Quadrature. Consider α , such as $\alpha \in [0; 1]$, we want a function D_i

Figure 4.15: Schema illustrating the blind spot.



Source: the authors.

as presented in Equation (4.23). The desired value of ρ is the root of Equation (4.24).

$$D_i(\alpha) = \rho, \text{ st } L_i(0, \rho) = \alpha L_i^{max} \quad (4.23)$$

$$L_i^{max} \alpha - L_i(0, \rho) = 0 \quad (4.24)$$

For a desired value of α , we can solve Equation (4.24) using Newton-Raphson. This provides a function D_i which can be used to calculate any position on the meridian profile, and its parameter relates directly with the size of the arc $(0, D_i(\alpha))$.

4.4.1.2 The Blind Spot

There is however another important detail that must be taken into consideration: the Blind Spot. The hole next to the vertex of the truncated cone is likely to occlude a certain arc on the meridian profile. This area reflects no patterns from the truncated cone towards the camera and is known as Blind Spot (Figure 4.15). This area is mostly determined by the topographer's working distance and truncated cone dimensions. This is important because no information can be extracted from this zone and it must be estimated by combining data from all the points at the first region of transition.

To calculate the blind spot arc we need to find the surface entry point. This is the point on the surface which reflects the apparatus entry point (Figure 4.15). For any point, the incident ray can be directly calculated with its position and the nodal point. Also, the normal and the reflected ray can be calculated using Equations 4.14 and 4.8. To check if

the reflected ray goes through the apparatus entry point. Then, the search for the surface entry point consists of a linear search with increasing values of ρ , followed by a binary search to better refine the result.

4.4.1.3 Building the Pattern

Starting from the previously found surface entry point, we calculate the position for the next regions of transitions. Once these points have been defined, we must evaluate the reflection at each one of them and then calculate where their reflection will hit the truncated cone. We simply mark this points on the cone profile and then set the color for the regions between consecutive intersections. We go by alternating the colors of consecutive intervals. It is important that the first interval (the one starting at the corneal surface entry point) to be white or it will blend with the rest of the blind spot, in case a black-and-white pattern is adopted.

In the particular case of the regular pattern, we have to assure that consecutive arcs after the blind spot have the same length. Hence, we obtain a regular pattern.

4.4.1.4 Inverse Sampling Summary

The steps of inverse sampling for creating controllable patterns can be summarized as:

1. Find blind spot.
2. Calculate the arcs on the surface of our meridian profile.
3. Raytrace to create the pattern.
4. Repeat steps 1 to 3 for each one of the meridians.

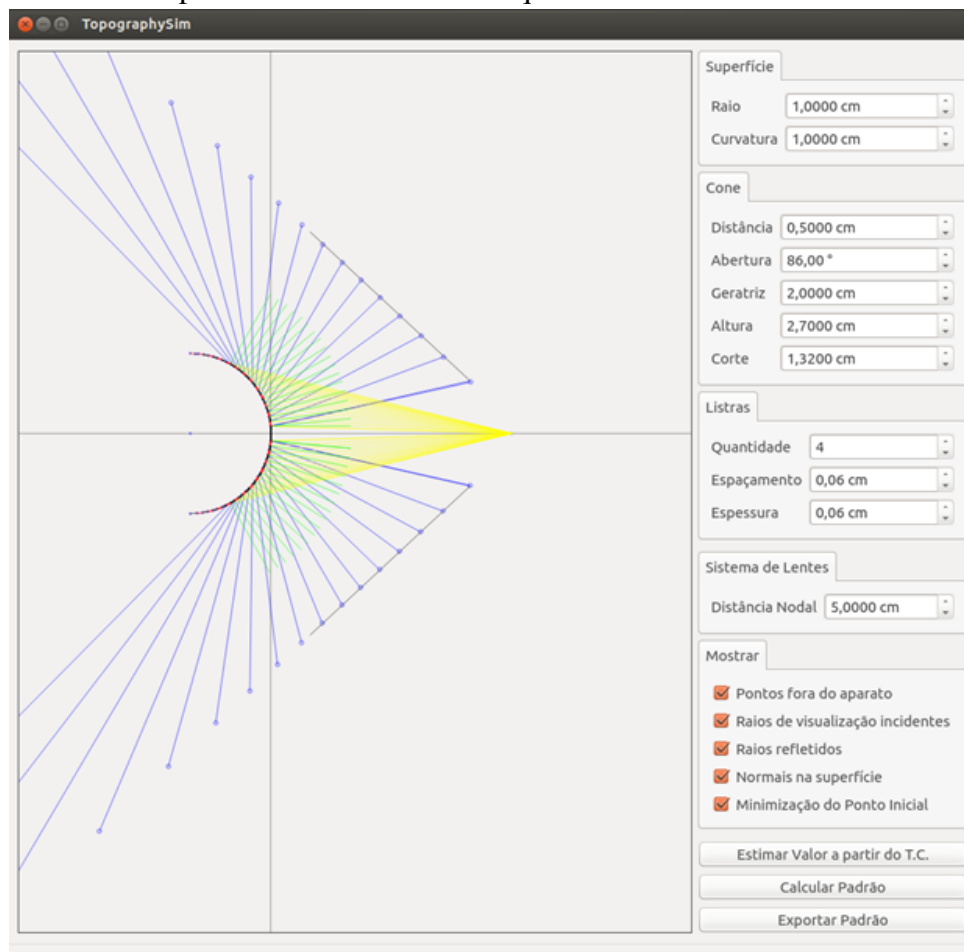
The inverse-sampling software developed to create arbitrary patterns can be seen in Figure 4.16.

4.5 Surface Data Reconstruction

The topography data is reconstructed from the segmented image generated by our simulated environment. The reconstruction is done by using the method of Callibration Spheres as described by Carvalho (), based on the method proposed by Halstead et al. ().

Consider our segmented image to have N regions of transition. They are in polar

Figure 4.16: Our controlled pattern creation software. Using this software it is possible to create controlled patterns and obtain data required to fabricate them.



Source: the authors.

coordinates (r, θ) , where r indicates the radial distance from the center. Let d_i be the radial distance from the center to the i_{th} region of transition in pixels.

The algorithm combines the information of a series of M calibration spheres to compose the intended data. It is important to note that each calibration sphere j has a known and constant radius of curvature C_j . We will fit the M values of d_i into a polynomial function $W_i(d)$ which maps a radial distance d (in pixels), to its corresponding radius of curvature (in millimeters). The function W_i is expressed in Equation (4.25). The fitting process consists in calculating the values of a_2 , a_1 and a_0 for all N different regions of transition. This is done by solving a linear system (Equation (4.26)) for each region of transition, where $d_{i,j}$ is the radial distance measured in the image of the calibration sphere i of the j_{th} region of transition. Those systems are solved using Least Squares.

$$W_i(\rho) = a_{2,i}\rho^2 + a_{1,i}\rho + a_{0,i} \quad (4.25)$$

$$\begin{bmatrix} d_{1,i}^2 & d_{1,i} & 1 \\ d_{2,i}^2 & d_{2,i} & 1 \\ d_{3,i}^2 & d_{3,i} & 1 \\ \vdots & \vdots & \vdots \\ d_{M,i}^2 & d_{M,i} & 1 \end{bmatrix} \begin{bmatrix} a_2 \\ a_1 \\ a_0 \end{bmatrix} = \begin{bmatrix} C_1 \\ C_2 \\ \vdots \\ C_M \end{bmatrix} \quad (4.26)$$

The choice of second degree polynomials was empirical, once it provides enough accuracy while providing very simple equations. Also, due to the rotational symmetry of the calibration spheres, the functions W_i may be applied to any reconstructed meridian.

Failures during the segmentation of the image or wrong estimates for d_i will compromise the solution of Equation (4.26).

Once the radius of curvature is reconstructed for the whole corneal surface, we can convert each sample data from Rc radius of curvature in mm to K axial power in diopters. It is done by using the formula in Equation (4.27), where n_c is the corneal refraction index 1.3375 (JACKSON,), n_{air} is the air's index of refraction, assumed as 1.0.

$$K = \frac{(n_c - n_{air})}{Rc} = \frac{0.3375}{Rc} \quad (4.27)$$

4.6 High-Level Data Extraction

Once the curvature data is reconstructed, we can display this information through circular color coded maps, as the one presented in Figure 4.2. Furthermore, additional information can be extracted from the data. In particular, we execute a process of simulated keratometry. It consists of calculating major curvatures and therefore the astigmatism error of a subject.

4.6.1 Color Maps

The first big consideration regarding the creation of a color map is the choice of which color should be assigned to each K value. There is no official standard for color assignment, which makes comparison between results from different commercial topographers quite non-intuitive. Smolek, Klyce and Hovis () proposes a Universal Standard Scale that is scientifically grounded and focused on optimizing the information provided by a color map.

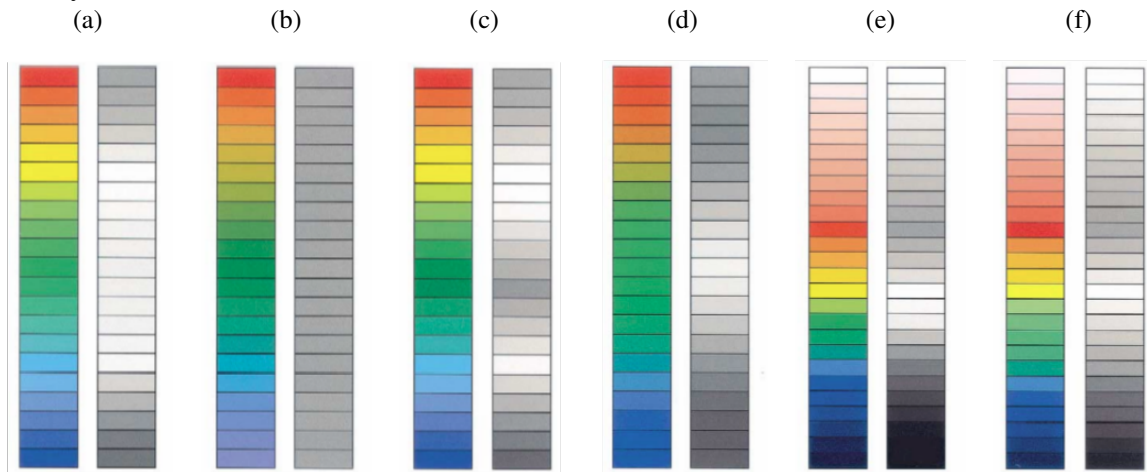
This color scale provides great contrast for most interesting cases, even when only grayscale output devices are available. It takes into consideration statistical distribution of possible subject's conditions when assigning colors to each K. The comparison of the Universal Standard Scale with other types can be seen in Figure 4.17. Note that all scales presented in Figure 4.17 meet the specifications of the American National Standards Institute and therefore can be used in commercial topographer solutions.

It is important to note that the reflected pattern is unlikely to be perfectly circular, nevertheless most color maps will be represented in a perfectly circular grid. Hence, to make our result easily interpretable by practitioners, a process of resampling must be put in place to distribute the values according to this grid. This is done by assigning the reconstructed values to their counterpart in a regular circular grid. Finally, a color map obtained for a simulated case can be seen in Figure 4.18.

4.6.2 Simulated Keratometry

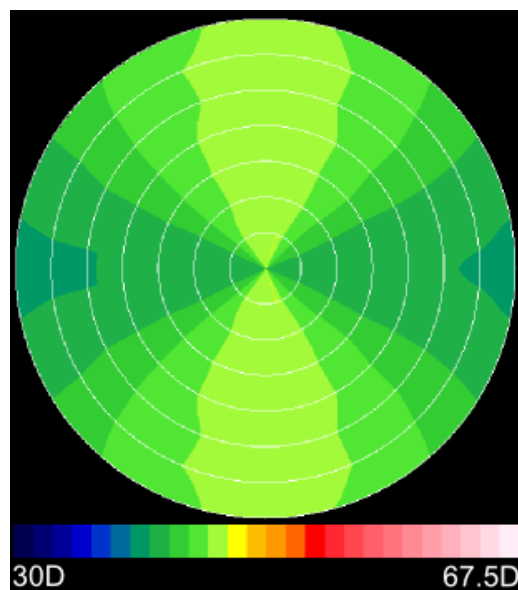
The keratometer has been for long considered to be the ancestor of the corneal topographer. It consists of estimating the main curvatures of a given surface. Since this

Figure 4.17: Different color scales that can be assigned to color maps and their corresponding grayscale versions: (a) ANSI H, (b) ANSI HL, (c) ANSI HLC, (d) ANSI RGB, (e) Klyce/Wilson and (f) Universal Standard Scale.



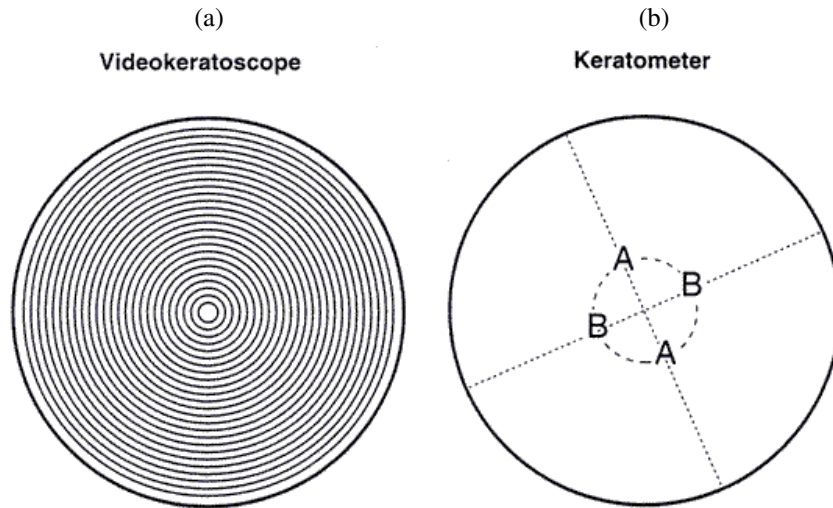
Source: extracted from Smolek, Klyce and Hovis ().

Figure 4.18: A color map for a simulated subject with $r_h = 8.44$ mm and $r_v = 7.50$ mm. It has 5D of astigmatism at 90° . The different white circles define different radial distance regions.



Source: the authors.

Figure 4.19: Representations of the corneal area covered by the topographer (videokeratoscope) and the keratometer. (a) The area covered by the reflection of the concentric circles from a corneal topographer. (b) The area covered by the keratometer and from where it extracts the main curvature data.



Source: Corbett, Rosen and O'Brart ().

information may vary significantly throughout the surface, it is usually calculated for specific radial distances. Figure 4.19 compares how the corneal data reconstruction done by a topographer relate to the data obtained by a keratometer. Note that both devices compute the same information of curvature, although using different approaches and also different samplings. For current eye care practice, keratometry is mainly used for assessing one's astigmatism condition.

Retrieving one's astigmatism consists of quantifying the corneal curvature at each meridian and finding the pair of meridians with the greatest discrepancy regarding their K axial power values (expressed in diopters), which also means finding the two principal curvatures of the corneal surface. In Figure 4.18 shows a series of concentric circles defining radial distances used for computing simulated keratometry.

The astigmatism value is defined as the difference between the main curvatures in diopters. There are two standards for expressing astigmatism (plus cylinder and minus cylinder), based on which of the main curvatures is used to describe the astigmatism axis.

5 THE CREATION OF A PROTOTYPE

We have defined our Topography Pipeline and also our desired topographer. We now present the building process of our physical prototype, which is a device that can be attached to the smartphone in order to perform the topography. Until now, we have dealt only with software solutions, in particular, they were focused in handling controlled and noise-free scenarios. There are huge challenges when working on these virtual cases, we show how we have addressed them and what could be the next steps to improve the topographer.

This chapter is dedicated to present the decisions made during the creation of our physical prototype, with emphasis on the challenges of imaging a corneal surface with the proposed hardware. We start by presenting the device we have built, going through the imaging process, and finally presenting the results obtained by using the device in the pipeline discussed in Chapter 4.

5.1 The Corneal Topographer Device

In order to perform the topography assessment in a real subject, we must build the physical device which works alongside the smartphone. This apparatus, together with the smartphone, is the hardware of our prototype. We will refer to this apparatus solely as our Corneal Topographer device.

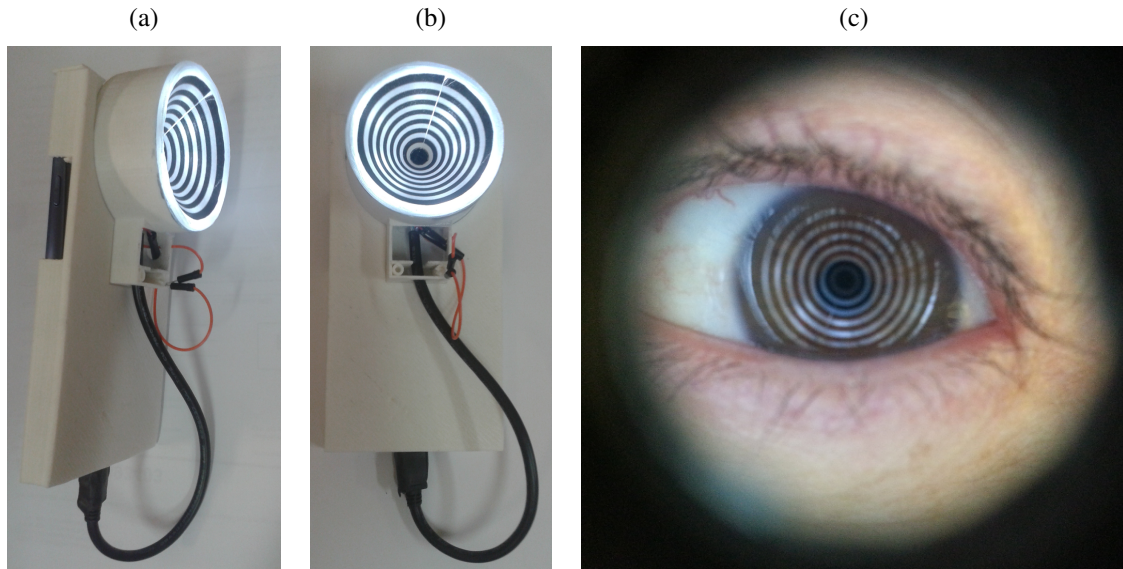
There are several functionalities that are expected to be supplied. First, it should assist the positioning of the subject's eye in the pre-defined working distance from the device. This distance may be defined by the optical system, or the device may be designed to support a target distance. The gadget is also responsible for the pattern to be reflected on the subject's cornea. A source light must be included in order to allow the reflection of the pattern clearly visible on the surface being assessed. Hence, the main components of the gadget that shall be put together are: **the outer shell**, **the cone** and **light source**.

These structures were modeled using the a 3D modelling software: Solid Works¹; and then printed by the three dimensional printer CL1². The printing process was done using polylactic acid, mostly known as PLA. This material is lightweight, resistant, biodegradable and derived from renewable sources. The printing process allowed for a high degree

¹<http://www.solidworks.com/> (Last visited 11/05/2015)

²<http://www.cliever.com.br/produto/impressora-3d-cliever-cl1-1> (Last visited 11/05/2015)

Figure 5.1: Prototype outer shell and its two main components. (a) and (b) show two views of the device, and (c) show the image captured by the smartphone camera.



Source: the authors.

of precision (accuracy of up to 1 mm thickness layer) while keeping iterative process quite flexible. Important to mention that later technology in 3D printing allow for ten to hundreds of times higher accuracy. However, those solutions are not as affordable as the one used in this project. Figure 5.1 depicts our corneal topographer prototype. Figure 5.1(c) shows an image captured with our prototype.

5.1.1 The Outer Shell

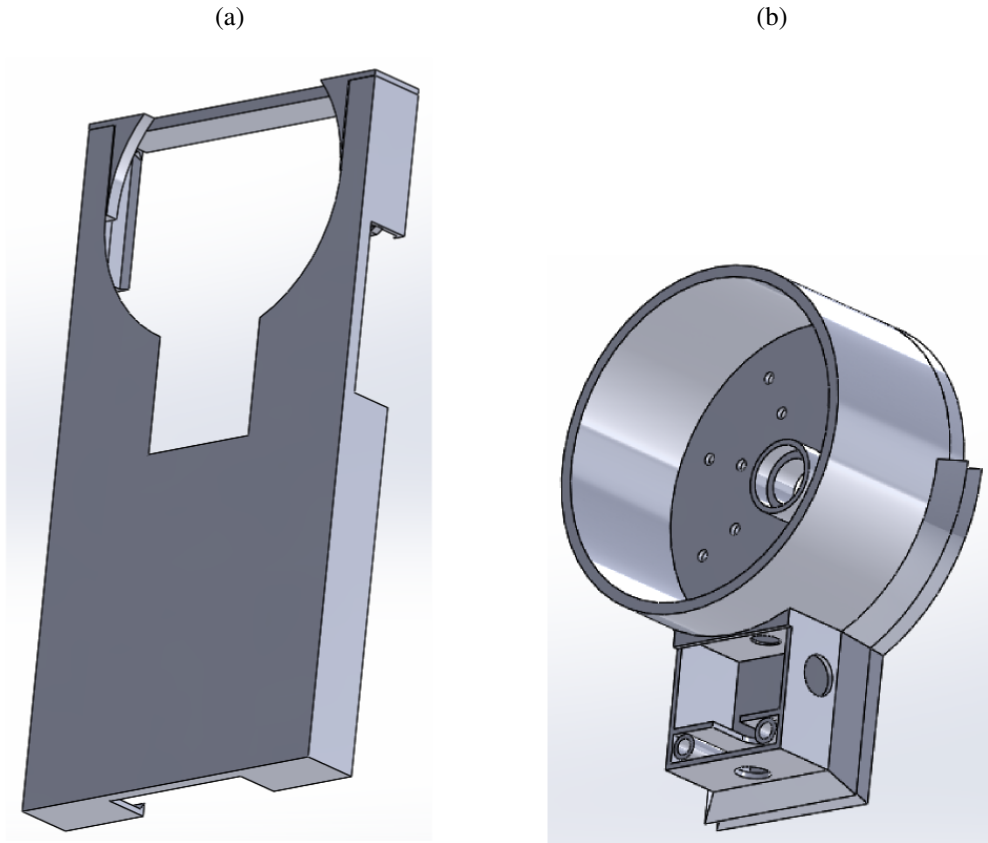
The outer shell structure was split in two components to allow the printing process to be feasible using our printer. The first component is a case which indeed is used to attach the smartphone to our prototype, see Figure 5.2(a). The second component is the core which provides structure to accommodate the cone and light source components (Figure 5.2(b)).

The case was designed as a simple smartphone case. It attaches to the smartphone due to a small detail in its borders (this can be seen in inset in Figure 5.3). The case was designed by taking into consideration the dimensions of the used smartphone (Samsung Galaxy 3^{TM3}).

These two components stick together due to a simple sliding system (Figure 5.4). We designed a small 'lid', that can be seen in Figure 5.5, to lock the core within the case

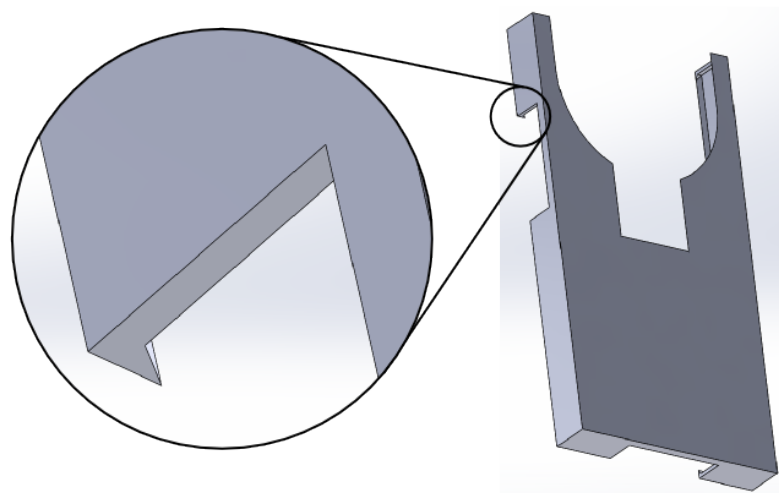
³<http://www.samsung.com/global/galaxys3/specifications.html> (Last visit 11/05/2015)

Figure 5.2: Prototype outer shell and its two main components. In (a) we can see the case that will enfold the smartphone, and in (b) we can see the core, which is going to be used as support for the cone and lighting sources.



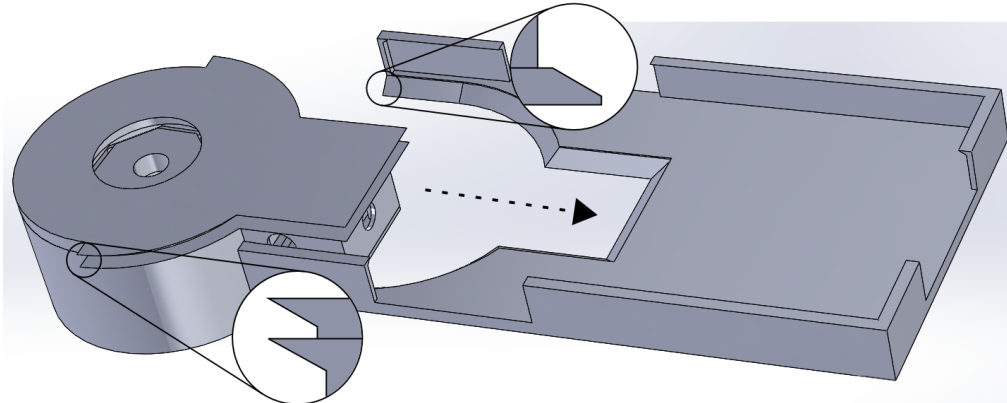
Source: the authors.

Figure 5.3: Outer shell case. The detail responsible for fixating the smartphone inside the case.



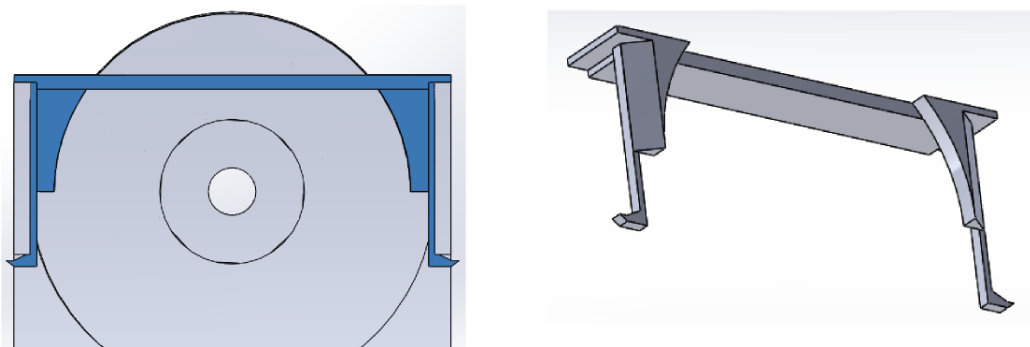
Source: the authors.

Figure 5.4: Outer shell components assembling through sliding. In the insets one can note the different profiles that allow for the sliding process and attaches the core to the case.



Source: the authors.

Figure 5.5: Outer shell case lid. This lid prevents the core piece to fall off after it has been inserted.



Source: the authors.

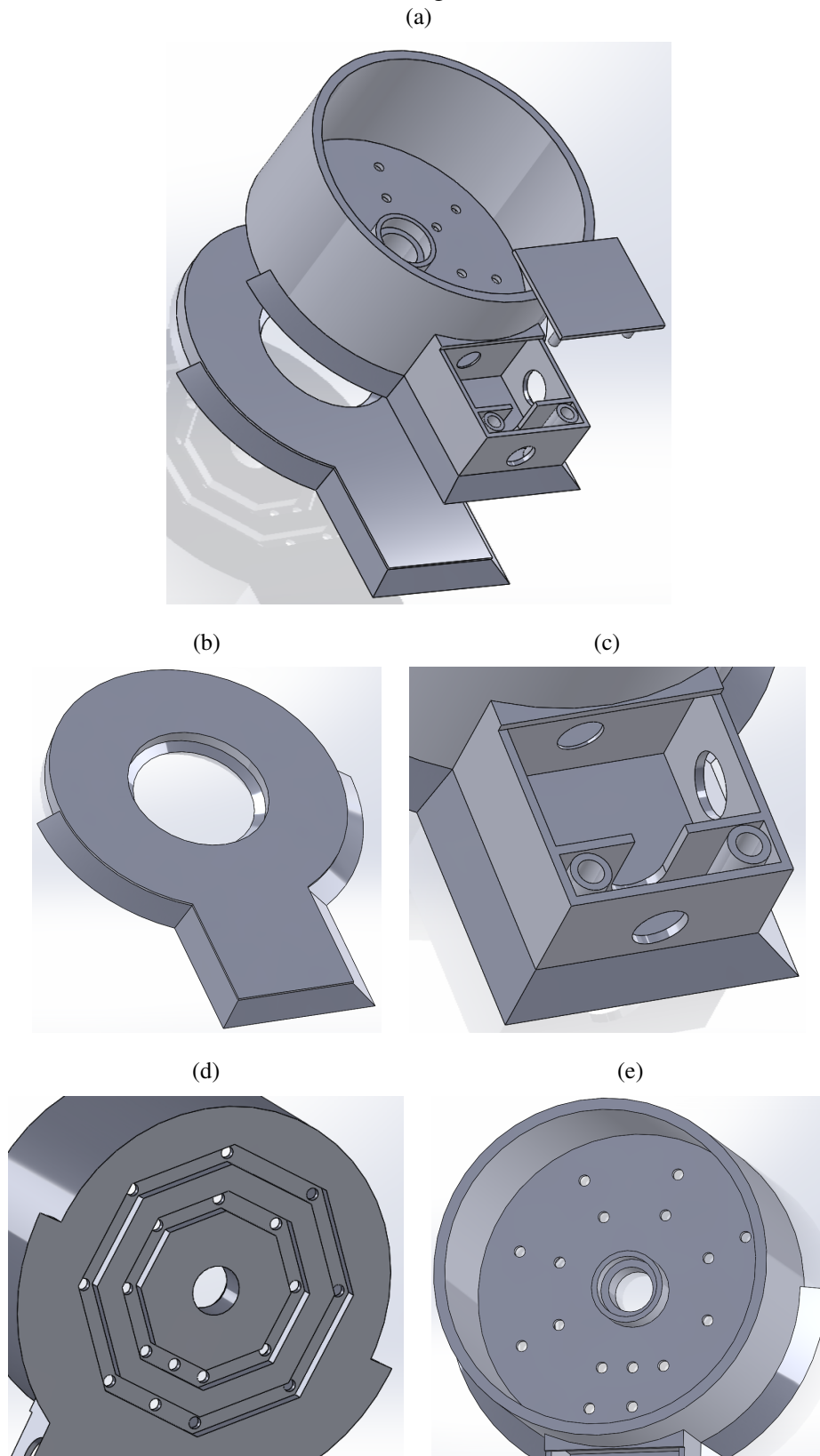
after sliding it.

The second component of the outer shell is its core. It is also composed of several pieces, as can be seen in Figure 5.6(a). Its structure positions almost all the functional components of the device. Those structures are: the cone, the lighting source, and the the magnifying lens. This lens is inserted in the piece seen in Figure 5.6(b). The small chamber in 5.6(c) is used to store wires and the On/Off switch for the lighting source. Figures 5.6(d) and 5.6(e) show the structures used to place the light source (6 white LEDs connected in parallel) and their wires. Finally, the base of the cone fits on the central hole depicted in Figure 5.6(e). The cone is hold in place by pressure.

5.1.2 The Cone

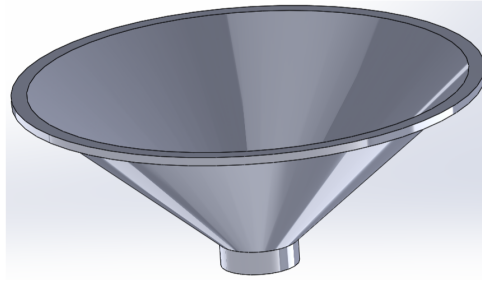
The outer shell is designed to properly accommodate the cone, the structure responsible for holding the Placido disk pattern. Differently from the other pieces, it had

Figure 5.6: Outer shell core and its components. (a) Inner components of the outer shell core. (b) A support responsible for holding the magnifying lens. (c) Small chamber used to hold wires from our light source, and the device's on/off switch. (d) The bottom of the core, showing grooves intended to hold the wires from our light source. (e) The main chamber of the core. The cone fits in its central hole. The smaller holes are used by the wires of the LEDs and a resistor used in the light source circuit.



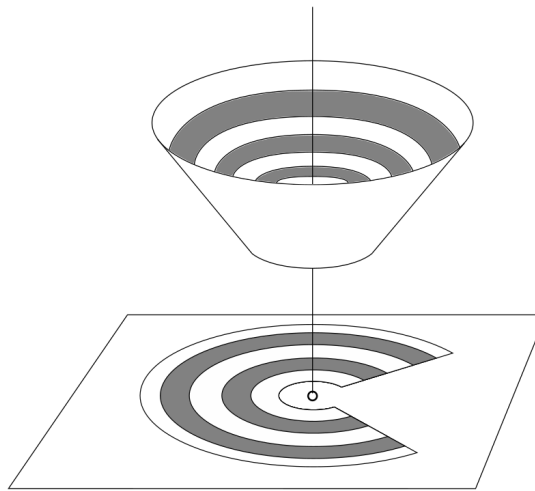
Source: the authors.

Figure 5.7: The cone designed to hold the Placido disk pattern and also to fit on the core component of the outer shell.



Source: the authors.

Figure 5.8: The cone blueprint creation process. It consists of creating a type of projection of the cone on a plane. The image created on the plane can then be printed in a regular laser or ink printer and then simply folded to achieve the intended cone.



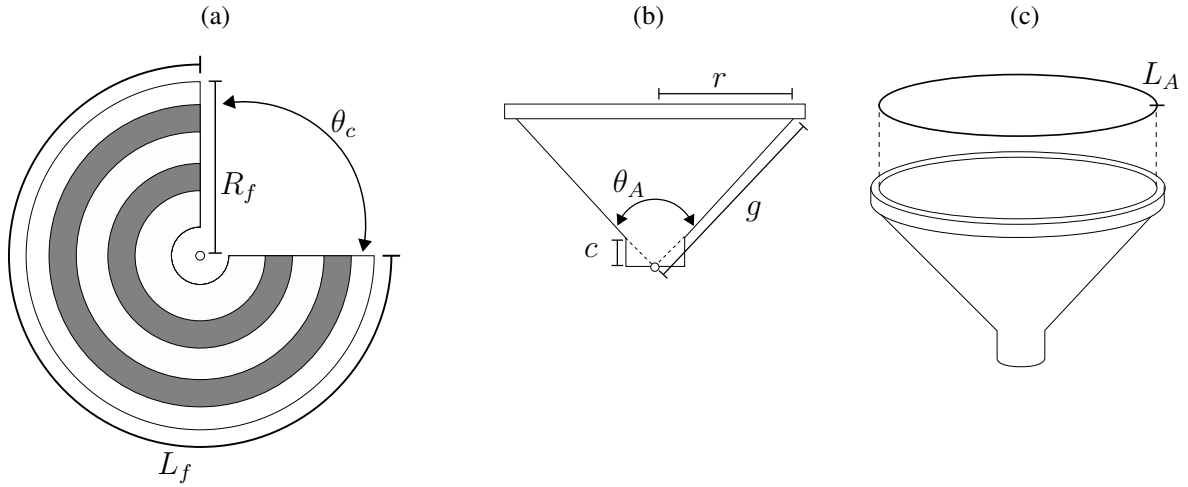
Source: the authors.

to be printed with a translucent PLA, to allow light to partially go through it. It ends up acting also as a light diffuser. Its design is shown in Figure 5.7.

As mentioned, the cone holds the Placido disk pattern. In the previous chapter, we introduced a simulation that can be used to create controlled patterns. We expanded it so that any designed pattern can be converted into a blueprint and, once printed on a regular ink or laser printer, it could be folded and directly placed on the inner surface of our cone. Figure 5.8 illustrates the idea of creating the pattern's blueprint.

The process of creating a blueprint is straightforward and can be done in multiple ways depending which parameters were used to define the desired cone. A cone blueprint is defined by three main variables: cone blueprint contour length L_f , cone blueprint radius R_f and angular cut size θ_c (Figure 5.9(a)). Following the schema from previous chapter, the cone is defined by a generatrix g , an aperture angle θ_A and a cut length c (Fig-

Figure 5.9: Cone blueprint properties and truncated cone schemas. (a) The cone blueprint. (b) and (c) A truncated cone and its main properties.



Source: the authors.

Figure 5.9(b)). Note that the generatrix must have equal size on the blueprint and it is the outer radius: $g = R_f$. Also, note that the external arc length of the blueprint must have the same length as the cone's main aperture (Figure 5.9(c)), therefore $L_f = L_A$. Their relations can be expressed by Equations 5.1, 5.2 and 5.3.

$$r = \sin\left(\frac{\theta_A}{2}\right) g \quad (5.1)$$

$$L_A = 2\pi r \quad (5.2)$$

$$L_f = (2\pi - \theta_c) R_f \quad (5.3)$$

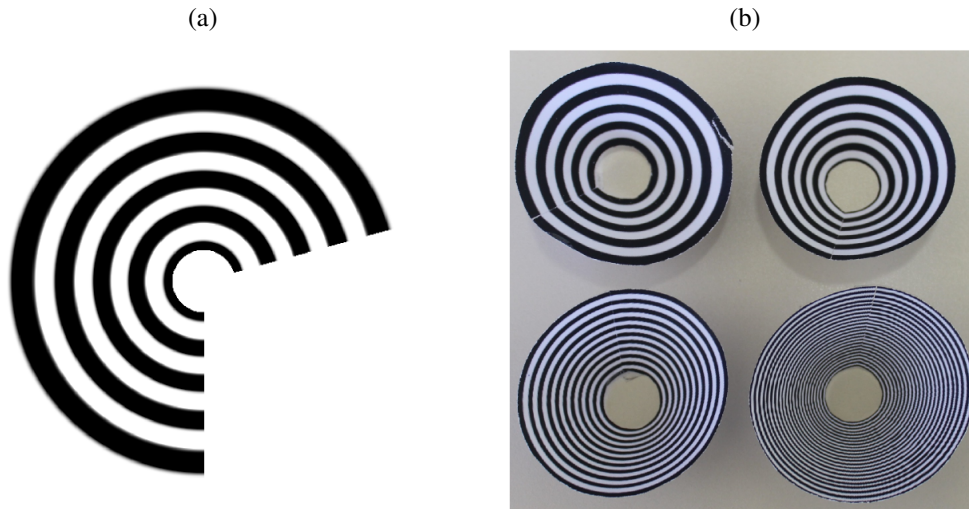
An example of a cone blueprint, ready to be printed, can be seen in Figure 5.10(a). In Figure 5.10(b) there are examples of folded cones using this blueprint creation process. To make it easier to put together the 3D translucent cone and the paper printed pattern, we used adhesive paper when printing the pattern.

5.1.3 The Light Source

The light source is a component of vital importance since it allows our imaging system (the smartphone camera coupled with our magnifying lens) to image the pattern reflection on the subject corneal surface.

We decided to use a set of six white LEDs connected in parallel (through struc-

Figure 5.10: Cone blueprint and actual printed and folded cone patterns. (a) a cone blueprint ready for printing, (b) examples of printed and folded Placido cone patterns.



Source: the authors.

tures on the bottom of the outer shell core). In order to improve the efficiency of the light distribution, we dyed the inner surfaces of the outer shell core with reflective silver painting. An important aspect of the light source is its energy source. Although we could have simply used external and portable batteries, we have modified the wiring of the mini USB cables in order to obtain energy directly from the smartphone's battery and therefore making our device lighter and relying only on its host smartphone.

5.2 Imaging Corneal Surfaces

The process of imaging a subject's cornea is the most error-prone process when performing topography assessment. It is during this stage that most of the noise is introduced in the sampled data, which can compromise the quality of the reconstruction and any information derived from it.

To expand the smartphone optical capabilities, we decided to incorporate a magnifying lens in our prototype. This lens allows the smartphone to image subjects from closer distances than it could by default. A convex lens with around 20D was used.

Before imaging any subject, there is a major point that should be handled. It is the optical distortion introduced by the smartphone's camera or by the external lens. To address this problem, we have used the Camera Calibration Toolbox for Matlab⁴, provided by Jean-Yves Bouguet. This toolbox provides several tools for evaluating an imaging

⁴http://www.vision.caltech.edu/bouguetj/calib_doc/ (Last visited 11/06/2015)

Figure 5.11: Calibration spheres used with their radii and dioptric curvatures (K values).



Source: the authors.

system optical distortion and also for correcting it.

But the reconstruction algorithm also needs calibration before assessing the subject. We used a series of commercial calibration spheres of known radii and K values (Figure 5.11). We used their holding structure to assure the desired working distance. Note that to acquire information from the calibration spheres, one must first segment them. This is a simpler problem than segmenting images of live subjects, once the calibration spheres do not contain any details on its surface that may interfere with the segmenting process.

The strategy adopted when imaging a corneal subject was placing the device in contact with the person's face, allowing better stability while ensuring the desired working distance (Figure 5.1(c) illustrates the result of the imaging process of a human eye).

5.3 Image Segmentation

After capturing a picture of a cornea exhibiting a reflected pattern (Figure 5.1 (c)), we need to process it to extract information for curvature reconstruction. This information

includes the center of the reflected circles, the radial distances (which are calculated from the center of reflected circles), and the iris area. The center of the reflected circles is important to calculate the radial distances. The radial distances, together with data from the calibration spheres, are used in the reconstruction algorithm. The segmentation of the iris is important for the computation of the simulated keratometry afterwards.

Even though commercial corneal topographers assess corneal data with high accuracy, there is very little public information provided by topographer's manufacturer. This presents a particular challenge for the community when investigating the topography image processing stage (FLORINDO et al.,). There are currently many approaches that can be taken in order to segment the imaged corneas (CARVALHO; BRUNO, ; CARVALHO; BRUNO, ; FLORINDO et al.,). Carvalho and Bruno () claim that the use of Marr-Hildreth filter provides better accuracy for the results.

It is important to keep in mind that most of the work done by the community on this subject was done by using images provided by the systems embedded in commercial topographers. These images are of high resolution and with considerably sharp edges. The images acquired by our prototype, however, do not have enough sharpness to be reliably handled by these methods. It happens mostly due to the camera of our prototype being slightly out of focus during the acquisition process.

5.3.1 Computing the Center of the Reflected Pattern

We propose an algorithm to retrieve the center of the reflected pattern. It needs an initial guess which is inferred assuming the subject cornea is quasi-aligned with our topographer. The algorithm improves our guess iteratively until it converges to the correct center. It is robust to failures of continuity of the circles.

The steps of the algorithm are:

1. Define a number N of directions $D_i \in [1^\circ; 180^\circ]$, $N \in [1; 180]$. The directions are uniformly distributed.
2. Create $2N$ rays and send from the current center guess C to opposite directions, organizing them in pairs with 180° between them.
3. For each pair of rays, calculate its intersection with the nearest circle borders on its two extremities.
4. Use the point halfway the two extremities of the previous intersection as a center

candidate C_c . The distance from this point to one of these extremities is the candidate radius R_c .

5. For each direction D_i , calculate its center candidate C_{ci} , calculate how good it is if chosen as the center for the nearest circle. This is done by calculating the difference between its R_{ci} and the distance from C_{ci} to all the points intersected at step 3.
6. Let C_i be the best C_{ci} from step 5. If $C_i = C$, C_i is our desired center; Otherwise, set C_i as the new center and go to step 2. The equality test is performed considering a tolerance.

5.4 Prototype Output

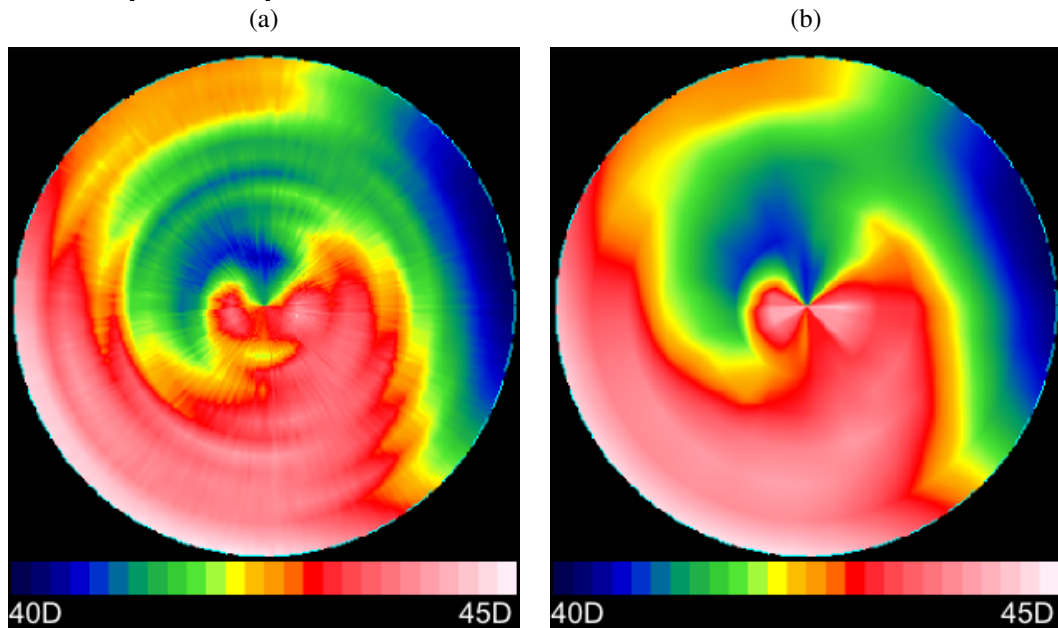
As discussed in the previous chapter, the reconstruction stage estimates a series of curvatures values which require some high-level data extraction approach in order to be better comprehensible and useful.

The data captured from a real cornea tend to be noisy, if compared to reconstructions of our simulated corneal surfaces. This is partially caused by the non-regularity of a corneal surface and also because there is error being introduced during the discretization of the data acquired (e.g., image discretization, discretization of the meridians). This creates high-level data proportionally inaccurate and uncomfortable for practitioners to work with.

Figure 5.12(a) and Figure 5.12(b) illustrate two color maps for the same reconstructed data. Note that in the first one the number of sample points used to generate the color map is forty times the number used in the second one. Although the first one is more detailed, it is not as simple to understand then the second, which may provide better insights for those analyzing it. Therefore, we put in place a Gaussian filter for the reconstructed data results which allows for smoother and more readable results (it is applied to curvature data before creating the color map). Considering that it is the overall shape of the cornea which is usually more important for a corneal topographer, our prototype sacrifices fine, detail in order to remove visual artifacts and achieve an improved readability.

Another important information that has to be extracted from the topography data is the simulated keratometry. In order to provide this information, we need the segmentation of the iris (Figure 5.13), which also defines the corneal region. We calculate this

Figure 5.12: Two color maps for the same data with different sampling density. (a) A color map that uses forty times the number of samples used in (b). The scale was normalized to the range $[40D; 45D]$ for both images.

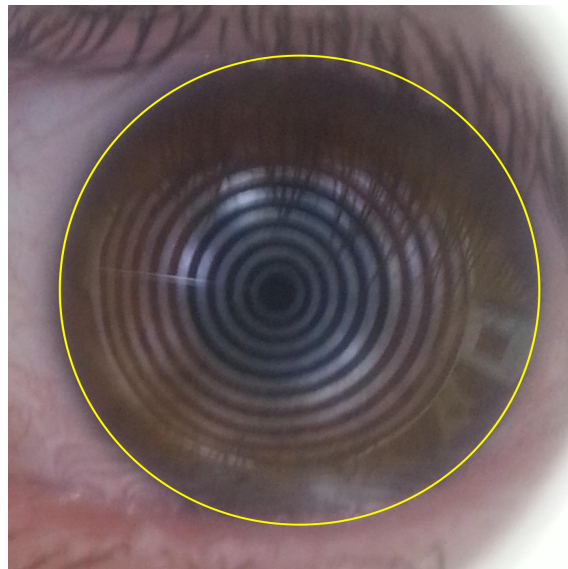


Source: the authors.

yellow bounding ellipse and the inscribed circle. We consider the average size of the iris, 12 mm (FORRESTER,), to be the same size as the diameter of this circle. Using this relation, we can extract the dioptric curvature for any specific radial distance on the sampled surface.

When computing the keratometry for radial distances between sampled regions, the data must be interpolated. To slightly reduce error, we interpolate data for a set of regions surrounding the desired radial distance and then average them. Ideally the keratometry will search for principal curvatures. But since the error may still compromise this search, we decided to enforce with-the-rule astigmatism. It is done by looking for pair of perpendicular meridians with higher curvature discrepancies.

Figure 5.13: Segmentation needed for simulated keratometry. Using the segmentation of this area, it is possible to compute the simulated keratometry for any desired radial distance.



Source: the authors.

6 RESULTS

Our results are divided in three major categories, each one reflecting a different type of subject investigated during the development cycle of this thesis. First, we discuss the virtual subjects evaluated using our simulation environment, which also serve to validate our Topography Pipeline. Second, we discuss the assessment of synthetic subjects using our prototype, while taking a set of calibration spheres as examples. Third, we discuss the data retrieved by our prototype through the assessment of human subjects.

It is important to notice that the reconstruction algorithm used in our pipeline has already been validated by previous works (HALSTEAD et al., ; CARVALHO,). Thus, we will focus on analyzing other aspects of the pipeline.

6.1 Virtual Subjects

The evaluation of a virtual subject is performed with the higher degree of control possible. The reconstructed data is expected to have accuracy at a micron scale due to the reconstruction algorithm used. For the experiments in this section, we used three simulated sphere of known radii: 7.50 mm, 8.44 mm, and 9.65 mm (Figure 6.1). Also, we used three virtual calibration spheres of radii 6.15 mm, 8.00 mm and 9.65 mm. Note that the chosen radii for the virtual calibration spheres match those real ones used by our prototype.

Consider K' to be the ground truth for a given K value. Since we are reconstructing spheres (constant curvature radius), it is reasonable to consider the average K value as a good representation for the reconstructed values. The resulting variance, average error and relative error of the K for each one of the simulated spheres can be seen in Table 6.1.

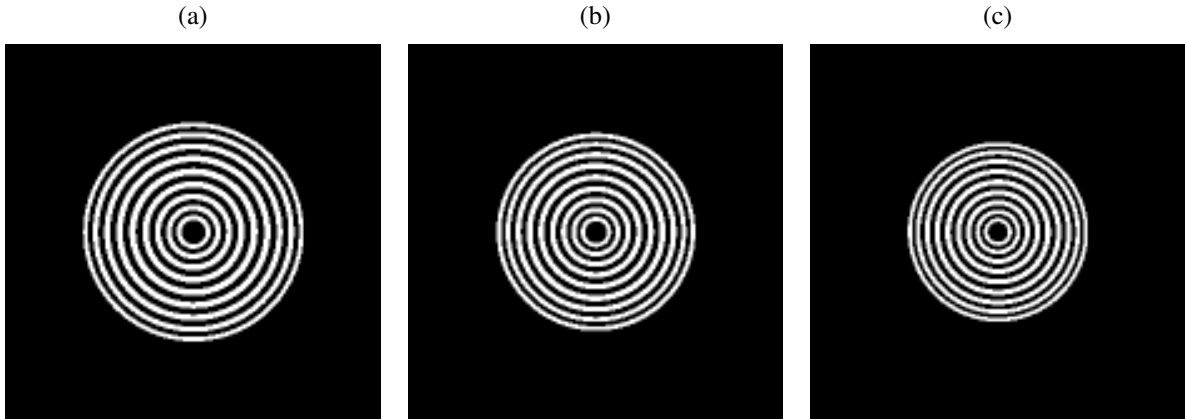
We evaluate the error in our pipeline when the subject is not properly positioned at the working distance of our topographer system. For this, we image each sphere five times in different positions, one of them being the correct working distance. This was done to

Table 6.1: Reconstruction of simulated spheres. K variance, average reconstructed value, average error and relative error for simulated spheres.

Sphere Radius	K'	Var. K	Avg. K	Avg. Error	Rel. Error
9.65 mm	35 D	0.0348	34.9866 D	0.0134 D	0.04 %
8.44 mm	40 D	0.0556	39.9882 D	0.0118 D	0.03 %
7.50 mm	45 D	0.1026	45.0085 D	0.0085 D	0.02 %

Source: the authors.

Figure 6.1: Imaging of three simulated spheres with radius: 9.65 mm (a), 8.44 mm (b) and 7.50 mm (c).



Source: the authors.

Table 6.2: K variance, average reconstructed value, average error and relative error for simulated subjects with $S_f = 0.9$.

Subject Radius	K'	Var. K	Avg. K	Avg. Error	Rel. Error
9.65 mm	35 D	0.0565	34.8589 D	0.1411 D	0.40 %
8.44 mm	40 D	0.0989	39.7764 D	0.2236 D	0.56 %
7.50 mm	45 D	0.1545	44.7596 D	0.2404 D	0.54 %

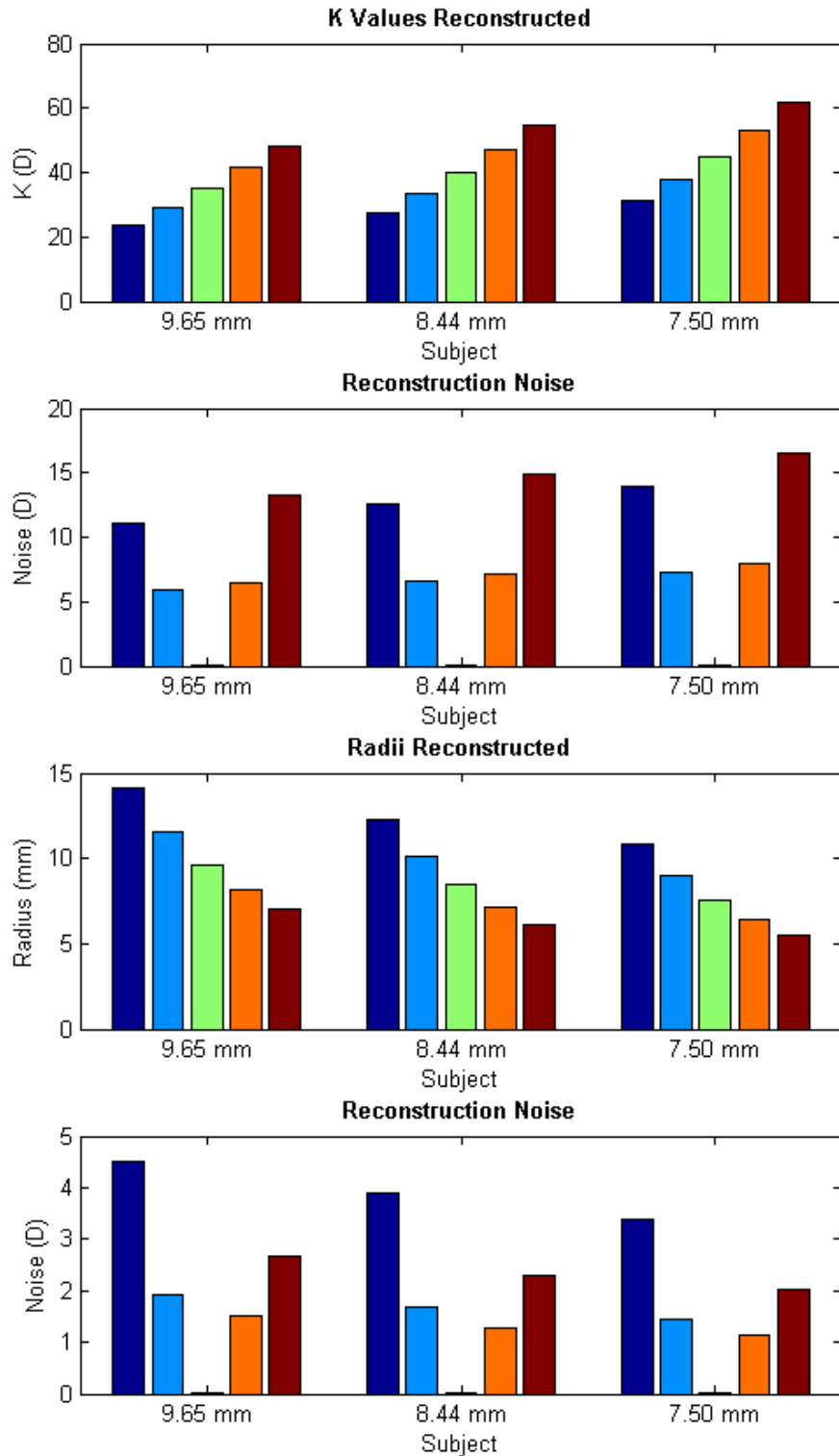
Source: the authors.

demonstrate that the error is reasonably proportional to the misplacing of our system. In Figure 6.2 we can see the comparison between computed average K values and radii for each virtual subject evaluation, the results are grouped by subject.

Next, we evaluate another important aspect of a virtual subject: the shape factor. When simulating spherical spheres we use shape factor $S_f = 1$. However, for more interesting tests it is necessary to simulate non-spherical surfaces. We are considering $S_f = 0.9$ to be a reasonable shape factor for human eyes (SALMON,). In Table 6.2 we present the K values obtained for the virtual corneal surfaces with same radii as before, but using a shape factor $S_f = 0.9$. Notice that the reconstruction error is quite larger, when compared to the precision of the reconstruction of the simulated spheres. This is directly caused by the use of a non-neutral shape factor ($S_f \neq 1$). This indicates that the reconstruction algorithms used has issues when dealing with non-spherical surfaces.

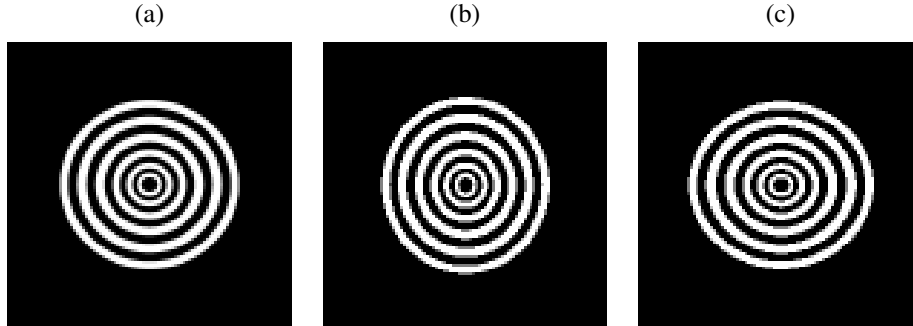
The last experiment with the simulation environment accounts for the reconstruction of simulated astigmatic subjects. We did three cases with different amounts of astigmatism. Also, we varied the shape factor for each one of them. Let A be a subject with $r_h = 8.0$ mm, $r_v = 7.5$ mm, $S_f = 0.85$ and $2.81D$ of astigmatism (SALMON,)(Figure 6.3(a)). Let B be a subject with $r_h = 7.5$ mm, $r_v = 8.04$ mm, $S_f = 0.85$ and $3D$ (Figure 6.3(b)). And let C be a subject with $r_h = 8.44$ mm, $r_v = 7.5$ mm, $S_f = 0.93$

Figure 6.2: Average K values obtained from the reconstruction of the simulated spheres varying the imaging distance. Note that the first two charts display the reconstruction result in Diopters and the other two as curvature radius in millimeters. Also that for each subject, the central bar corresponds to the value reconstructed at the proper working distance.



Source: the authors.

Figure 6.3: Three simulated subjects with astigmatism. The subject A (a) has $r_h = 8.0$ mm, $r_v = 7.5$ mm, $S_f = 0.85$ and $2.81D$ of astigmatism. The subject B (b) has $r_h = 7.5$ mm, $r_v = 8.04$ mm, $S_f = 0.96$ and $3D$ of astigmatism. The subject C (c) has $r_h = 8.44$ mm, $r_v = 7.5$ mm, $S_f = 0.93$ and $5D$.



Source: the authors.

Table 6.3: K value reconstruction for astigmatic simulated subjects with non-neutral value of shape factor (non-spherical surfaces).

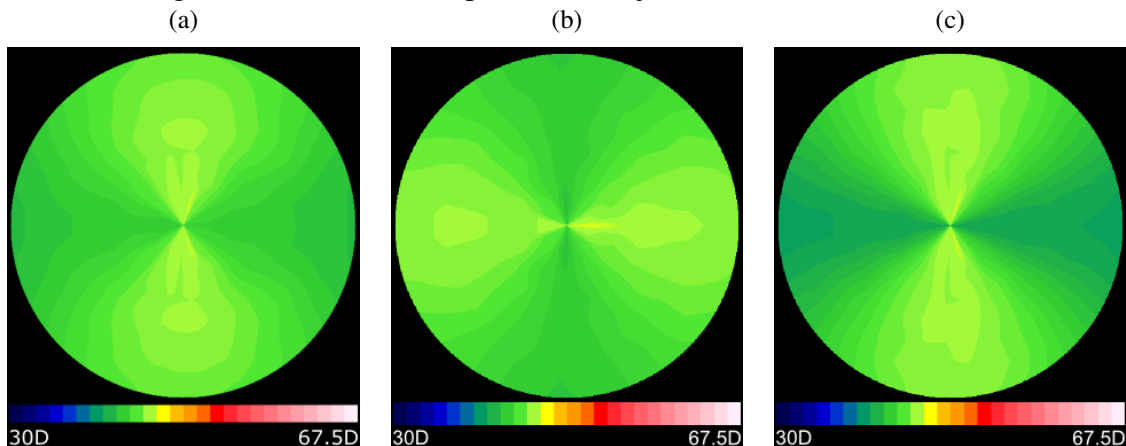
Subject	K'_1	Avg. K_1	K'_2	Avg. K_2	Astigmatism Error	Rel. Error
A	42.2 D	41.9171 D	45 D	44.5801 D	0.1370 D	4.90 %
B	45 D	45.1482 D	42 D	41.8000 D	0.3482 D	11.61 %
C	40 D	39.9494 D	45 D	44.7312 D	0.2182 D	4.36 %

Source: the authors.

and $5D$ (Figure 6.3(c)).

Consider K_1 to be the average K value at meridian 0° and K_2 to be the K value at meridian 90° . Let K'_1 and K'_2 be the ground truths for K_1 and K_2 , respectively. Table 6.3 shows the average of the obtained reconstruction values. The absolute error seems to be confined within the ones obtained for subjects with shape factor $S_f = 0.9$. The color maps referring to those subjects can be seen in Figure 6.4. Notice how the color pattern easily indicates the axis of main curvature.

Figure 6.4: The color maps for the subjects A (a), B (b) and C (c).



Source: the authors.

Table 6.4: K values reconstructed for the callibration spheres.

Sphere Radius	K'	Var. K	Avg. K	Avg. Error	Rel. Error
9.65 mm	35 D	0.0250	34.9909 D	0.0091 D	0.03 %
8.00 mm	42.2 D	0.2663	42.2294 D	0.0294 D	0.07 %
6.15 mm	54.9 D	1.3390	54.9683 D	0.0740 D	0.14 %

Source: the authors.

Regarding the simulation of subjects and their evaluation, our system achieved high accuracy. It is at micron scale for the reconstruction of regular spherical surfaces, and it is still a good estimation for non-spherical surfaces as well. Although, we have also observed that when non-spherical surfaces are used, there is non-negligible growth of the error. This has an important influence on the precision of the astigmatism estimation.

6.2 Synthetic Subjects

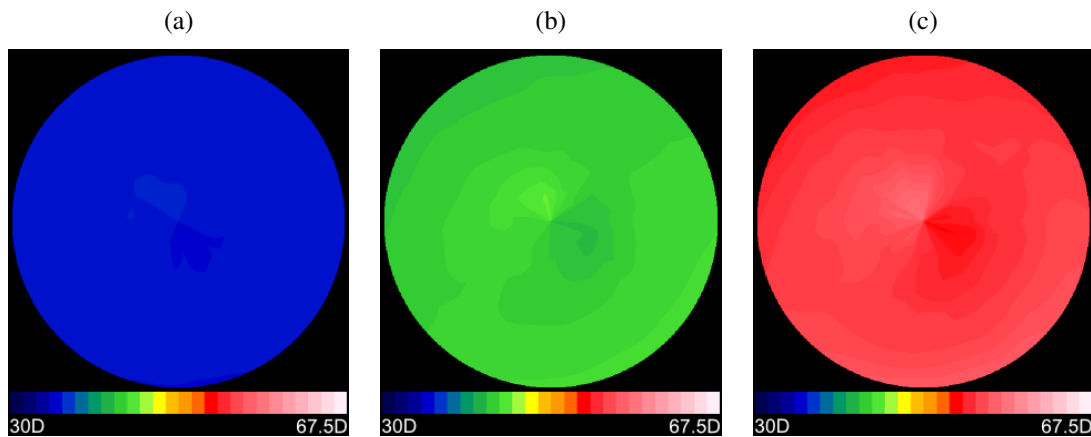
The use of calibration spheres of known radius is the traditional approach to evaluate a topographer's performance. Commercial solutions often include sets of these spheres to help them keeping the device calibrated. The ones used during the development of this thesis can be seen in Figure 5.11. In the previous chapter, we presented how we acquired data from them. Following, we discuss how we can use them as synthetic subjects for the reconstruction process.

The used reconstruction algorithm is an approximation. Therefore, even when evaluating the same real calibration spheres used on its calibration, some inaccuracy is still expected. It is reasonable to see these cases as the highest accuracy our prototype would be able to achieve using this reconstruction approach. The variance, average, error and relative error of the K values reconstructed can be seen in Table 6.4.

Notice that the reconstruction of our real calibration spheres has provided accurate global information, with a precision similar to the one obtained in our simulated environment. Nevertheless, when analyzing their color maps, we note that there is marginal error in the output, as can be seen in Figure 6.5.

The results obtained by these synthetic cases enforce our claim that our device is an interesting option for screening subjects. Although it lacks precision in several regions of the sampled surfaced, it is capable of correctly estimating global information about the subjects (in this case, the subjects sphere radii). In addition, the results presented in the color maps also strongly indicate that there are major issues that must be fixed regarding the effective accuracy of our device when dealing with spherical regular surfaces. Since

Figure 6.5: Color maps for the reconstruct synthetic cases. They were created using the USS absolute scale. Their curvature radius are: (a) 9.65 mm, (b) 8.0 mm, and (c) 6.15 mm.



Source: the authors.

the same reconstruction process provides higher accuracy for simulated cases, it indicates that the imaging process is the most critical step of our Topography Pipeline, and the natural choice for future enhancements.

6.3 Human Subjects

The most important validation is the assessment of the prototype's performance when dealing with real corneas. However, it is also the most complicated assessment to perform. Mostly because there is no ground truth for the geometry of a subject cornea.

Topographer devices have autonomy to work on slightly different regions of the corneal surface. Moreover, their most common outputs, the color maps, are not created using any standard color scales (there are some ANSI regulations, but they are not enough constraining (SMOLEK; KLYCE; HOVIS,)), which makes comparisons between color maps from different devices subjective and inaccurate. Nevertheless, we are still going to present color maps created by our prototype and compare them with data from a commercial solution for corneal assessment, due to the importance of corneal maps as a result of the corneal topography.

On the other hand, the simulated keratometry consists of objective information provided by a topographer device, and is expected to be reasonably similar when assessed by different devices on the same subject. Therefore, it is an objective information for comparing with our results.

The discussion of our results for human subjects is therefore divided in two main

stages. First, we subjectively compare the color maps we created against ones provided by commercial solutions. Second, we compare our simulated keratometry data against data obtained from other devices.

The evaluation of our prototype included 6 human subjects, ages ranging from 20 to 26, consisting of 12 human corneas. We assessed each individual cornea 3 times, performing a total of 36 corneal assessments with our prototype.

As previously discussed, our acquisition process is not yet optimal. Traditional segmentation approaches for Placido images failed to extract reasonable data from our samples. Hereby we present the results obtained through a manual segmentation process, which can be seen as the ground truth segmentation for the data we obtained. We have not achieved the same accuracy in segmentation by an algorithmic approach yet. Thus, the following results are representative of what can be achieved with our prototype. Keep in mind that our Topography Pipeline enforces modularity and other segmentation approaches can be integrated in the future.

6.3.1 Color Maps Comparison

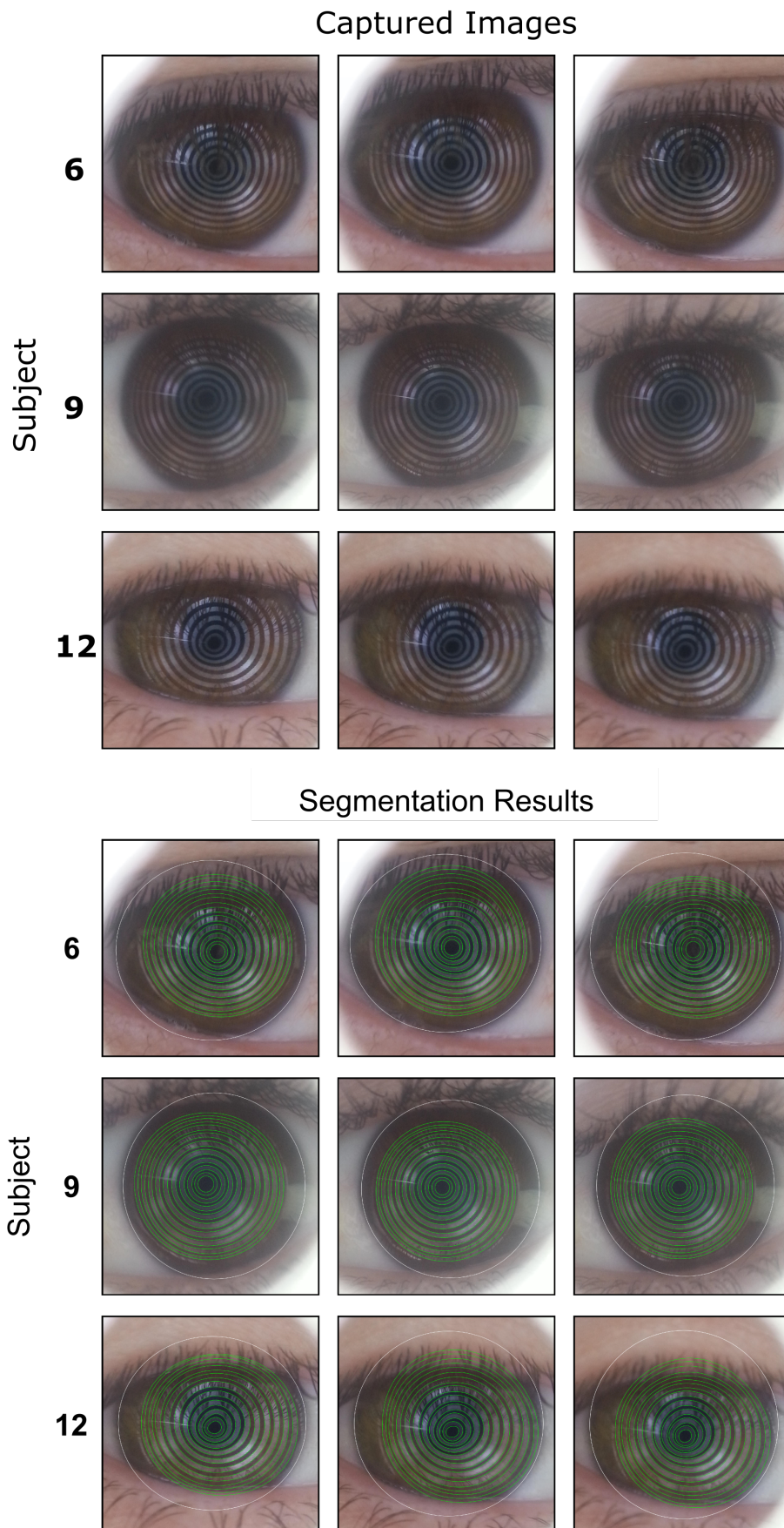
Following, we evaluate the color maps generated by our prototype. We start by presenting the data originally imaged and their corresponding segmentation. Afterwards, we analyze the error of our imaging process through the use of a different type of color map, which we will be calling *difference map*.

We have chosen to present the results for a subset of our data, containing some of our most interesting results¹. We have chosen the subset containing the corneal subjects 6, 9 and 12. These represent three major range of results obtained by our prototype: a very good accurate reconstruction (subject 6), a poor approximation (subject 9) and a considerably accurate case but with non-negligible error (subject 12). The imaged subjects and the corresponding segmentations of the reflected pattern can be seen in Figure 6.6.

In order to ease the comparison of the generated color maps, we created the difference map D_m . Let C_1 , C_2 and C_3 be our three curvature evaluations for the same subject. The difference map D_m is defined by Equation (6.1). The obtained color maps can be seen in Figure 6.7. Note that most cases have very low amount of differences and that the

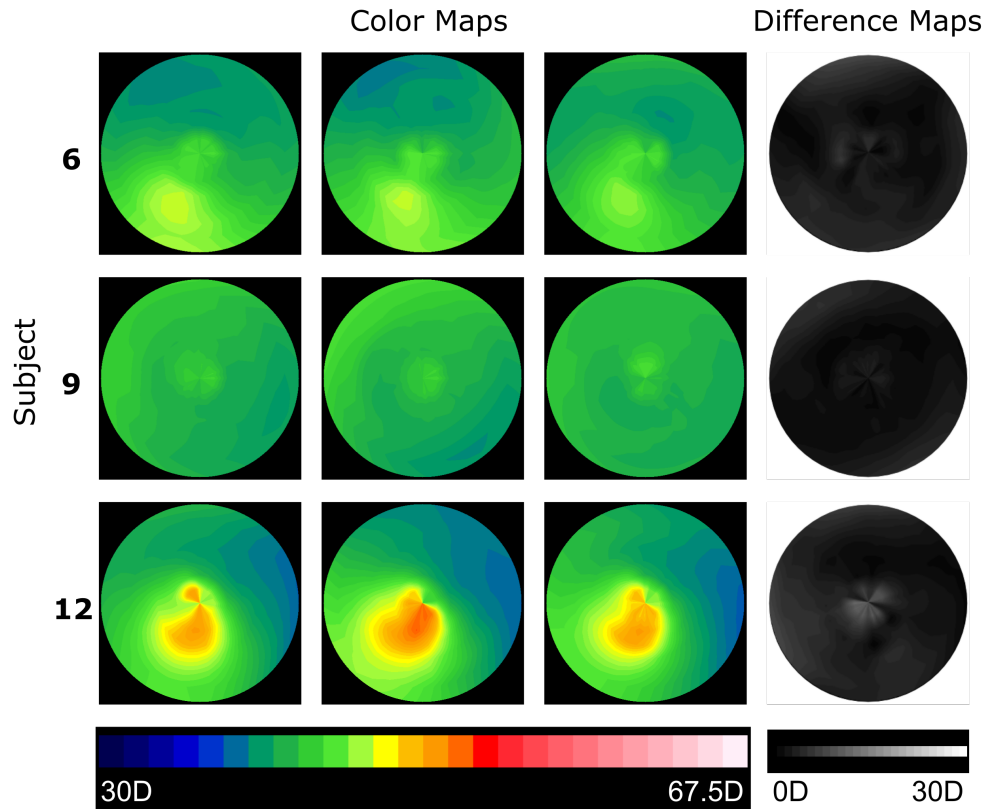
¹Note that our full dataset containing the reconstruction data of all our 12 corneal subjects can be downloaded at the Internet in the link: <https://goo.gl/JTTPCL>.

Figure 6.6: The acquisition process and the segmentation used.



Source: the authors.

Figure 6.7: Difference maps derived from the color maps generated by our prototype.



Source: the authors.

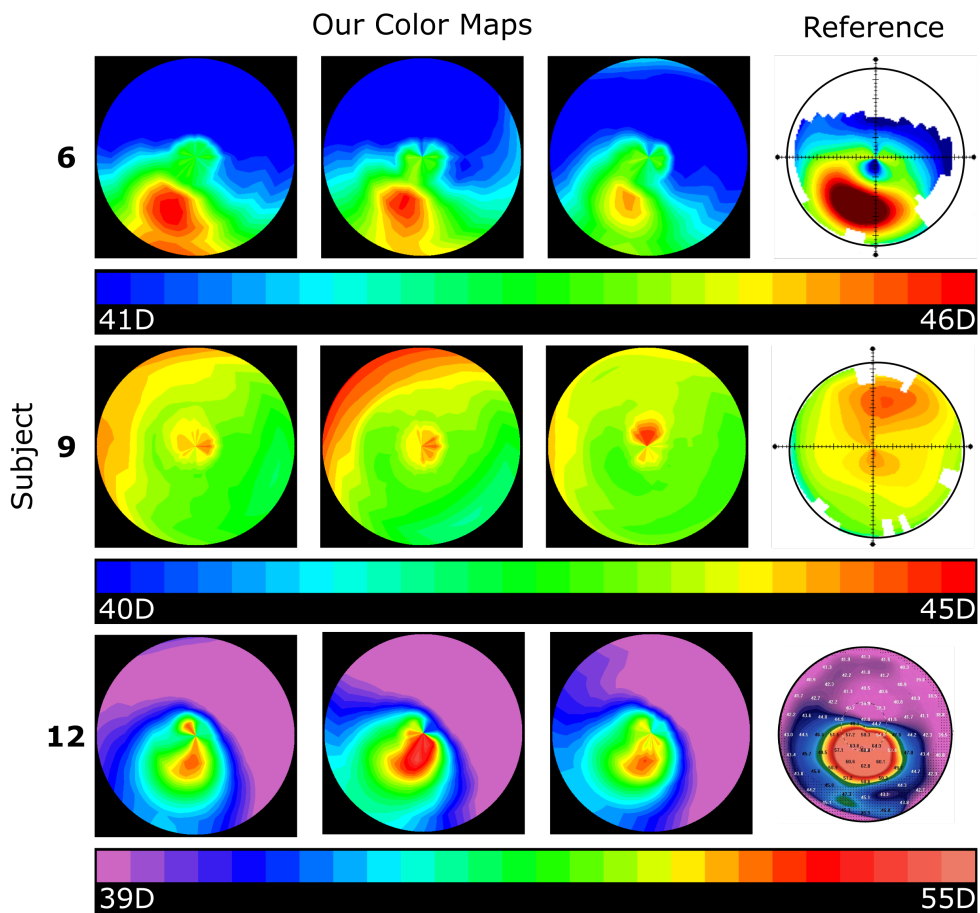
case with higher amount is the one with higher K-value variations within its samples.

$$D_m = |C_1 - C_2| + |C_3 - C_2| + |C_3 - C_1| \quad (6.1)$$

We now present the evaluation of the generated color maps against reference data from commercial devices. To make this comparison clear and easier, we changed the color scale of our color maps. Therefore, instead of using the universal standard scale, for each comparison, we used the same color scale used by the commercial device. These comparisons can be seen in Figure 6.8.

Note that our color maps express reasonably similar informations. Although, they have overall differences regarding their K values, that is likely to have been caused by noise during the imaging process.

Figure 6.8: Color maps generated by our prototype against their respective reference map. The reference color maps in the first two rows were obtained with a Topcon KR-8000PA corneal topographer. The reference color map in the third row was generated using an Oculus Pentacam².



Source: the authors.

6.3.2 Simulated Keratometry Evaluation

The simulated keratometry provides objective data which can be easily compared. It measures the main curvatures, whose differences quantifies a subject's astigmatism. Those curvatures can be both represented as radius of curvature R in millimeters or as K axial curvature power in diopters. Let R_1 and R_2 be the main radius curvatures and K_1 and K_2 be the main axial curvatures obtained by our prototype. Since these values may vary throughout the corneal surface, we decided to work with the central region of the cornea, covering 3 mm of diameter.

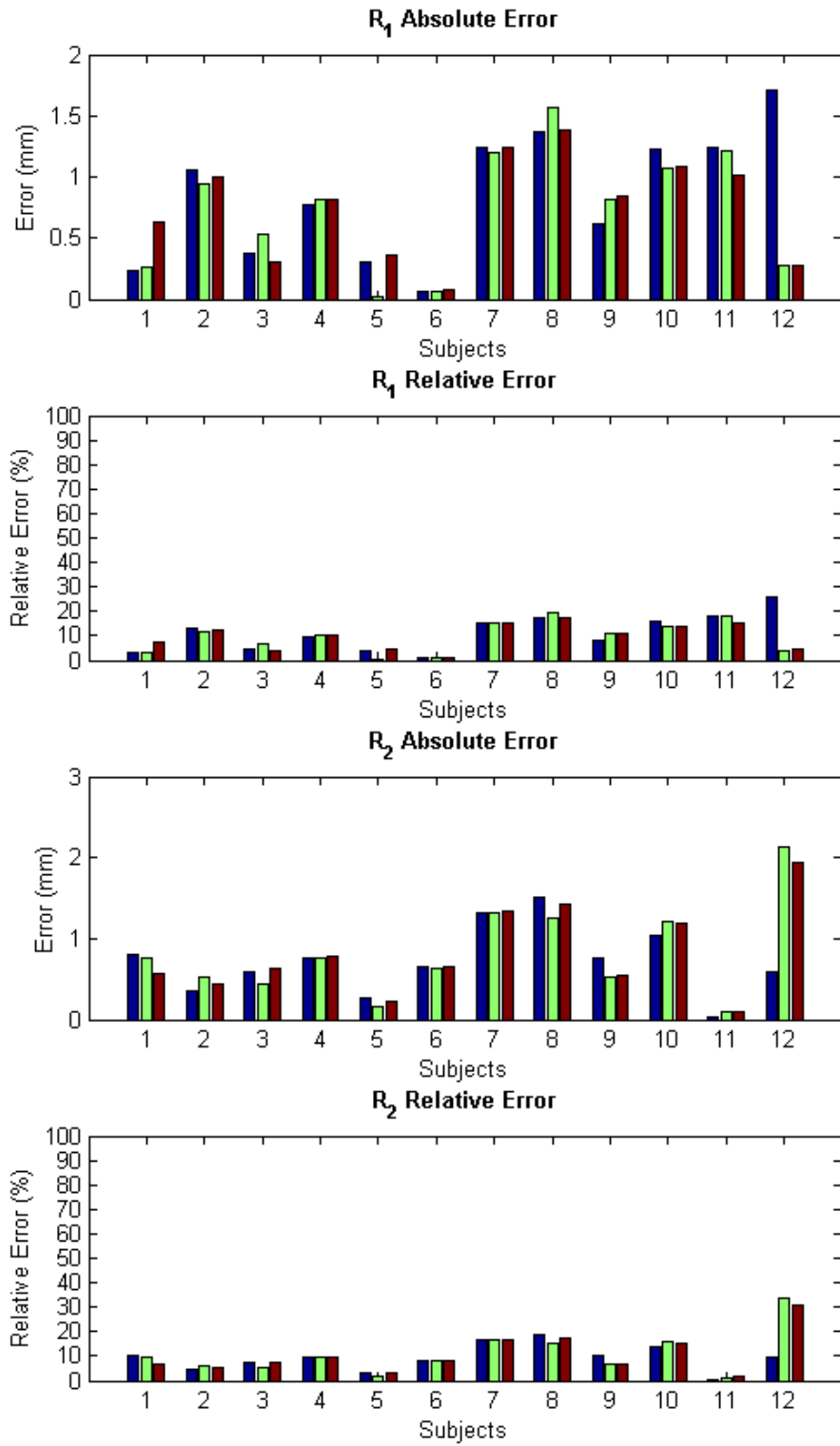
The values of curvature radius were reconstructed for each of the 36 corneal assessments. The error found in this data when compared with the ones from commercial solutions can be seen in Figure 6.9 (their results being grouped by their corresponding subject). We can see that most of the subject's radius-absolute-error remained around 1 mm. But it is important to notice that the relative error was lower than 8.23% for the R_1 and 8.47% for R_2 . Which indicates a substantial amount of precision. Figure 6.10 presents the error for reconstructed K values of main curvatures. Our tests achieved an average K_1 relative error of 9.5% and an average K_2 relative error of 9.0%.

The reconstruction values for the R 's and K 's both indicate that the values obtained are close to the expected (from the tests on the simulation environment), but their error have considerable influence in the estimation of the simulated keratometry. Also, notice that for the same subject, there was non-negligible variability in the error.

Figure 6.11 presents the error in astigmatism estimation by our device. When analysing the results, a curious pattern was observed: corneal subjects with higher astigmatism error (subjects 5, 6, 11 and 12) are cases clinically diagnosed as keratoconus. Subjects 5 and 6 being at earlier stages. Subjects 11 and 12 currently under contention treatment. This observation suggests that our prototype can potentially be used for screening patients with keratoconus.

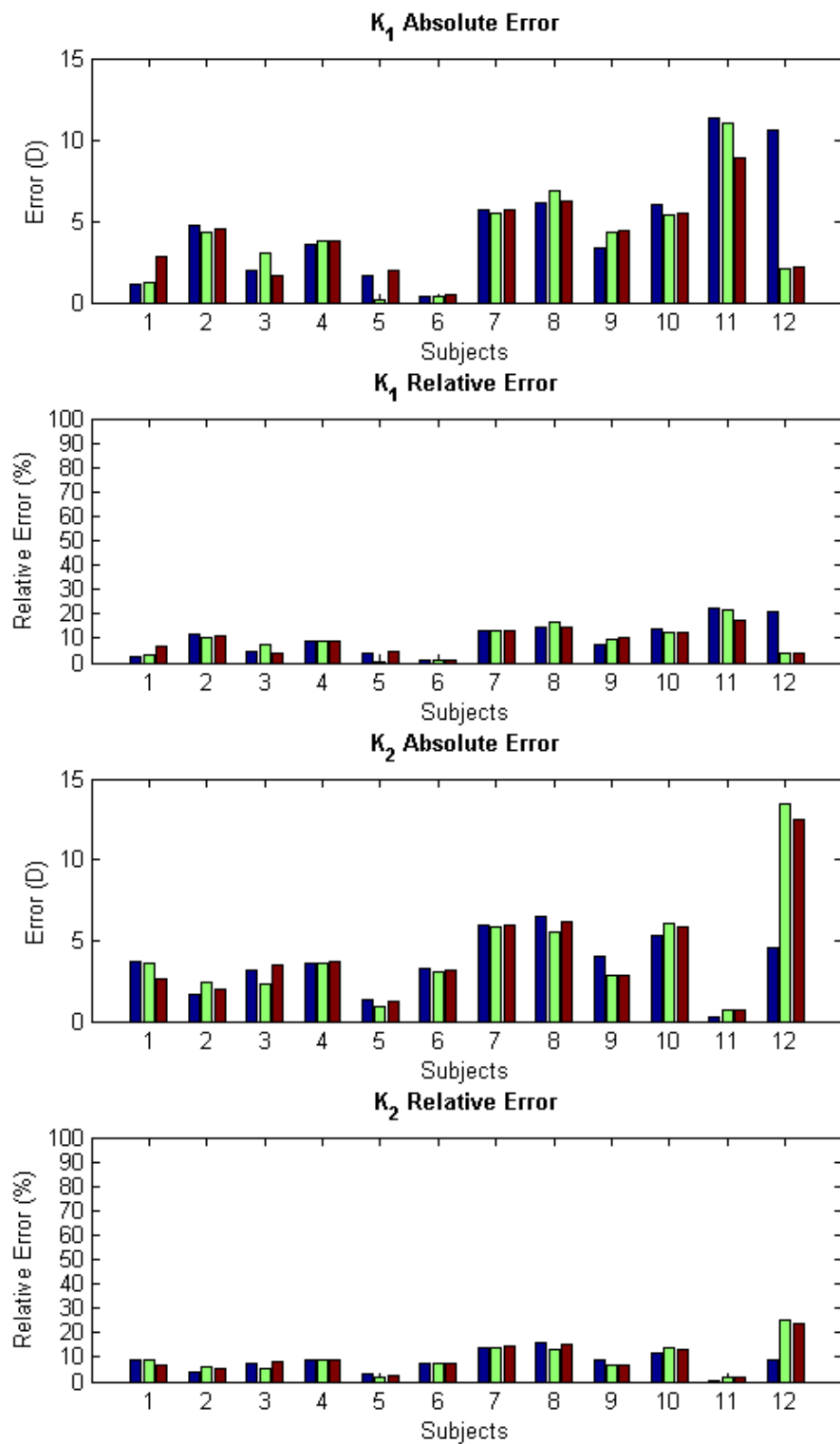
Note that our full dataset of reconstructed keratometry data can be downloaded at the Internet in the link: <https://goo.gl/JTTPCL>.

Figure 6.9: Main radius-of-curvature reconstruction error for 12 human subjects. The colors indicate the three assessments.



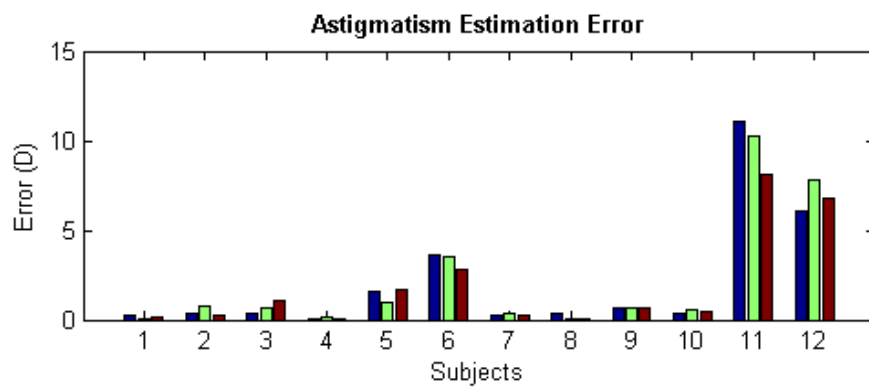
Source: the authors.

Figure 6.10: Main axial-curvatures reconstructions error for 12 human subjects. The colors indicate the three assessments.



Source: the authors.

Figure 6.11: Astigmatism error estimation for human subjects.



Source: the authors.

7 CONCLUSIONS AND FUTURE WORK

We have presented throughout this thesis a discussion about the creation of a low-cost corneal topographer. We describe a *Topography Pipeline* that is straightforward and can be used as a guide to the development of a corneal topographer. A system that follows this pipeline, should be able to modularly incorporate different techniques and approaches from the domain of corneal topography.

We presented a simulation of the whole corneal topography assessment of a virtual subject modeled as an ellipsotopic surface using a Placido-disk-based topographer. We propose two strategies for imaging this surface: the *Radial Sampling* and the *General Sampling*. We proposed the idea of a *Controlled Pattern* that can be created using our *Inverse Sampling* approach.

The *Prototype* presented is *easily reproducible* without requiring a big budget. It requires a 3d printer that can be an entry level printer (as the one we used). For creating the pattern, a regular laser printer can be used. On the core, a smartphone is required, almost any of them can be used.

However, as we presented in our results, there is still a lot of room for improvements. The prototype itself can be enhanced, so the working distance is assured in a more reliable fashion. Moreover, its optical system requires a complete redesign so traditional segmentation techniques can be used for the images captured by it.

Results obtained with the reconstruction of virtual non-spherical surfaces suggests that the algorithm of calibration spheres loses some precision when reconstructing virtual surfaces that diverge from the ones used for callibration. Variations of about 10% of the ellipsotopic shape factor led to a ten-times increase in the error of the reconstructed K values. Nevertheless, these errors remained below 0.25D, which is an acceptable precision.

The results for the assessment of human corneal subjects have shown that the present prototype's faults are not negligible. It achieves considerable precision on its color maps, by providing the most important aspects present on the reference color maps. However, for the simulated keratometry, it did not achieved the same level of accuracy. Hence, we believe that our current prototype has potential as a screening tool, but it is not ready yet to replace commercial topographers in clinical use.

Overall, we believe to have created a cohesive set of guidelines and discussed the main issues required for studying the subject and building low-cost corneal topographer devices.

7.1 Future Work

Following, we present some ideas that we believe should be explored in the future since they have the potential to greatly enhance the creation of low-cost corneal topographers.

Expanding the ellipsotopic model so more complex features can be simulated on a virtual subject, should allow for deeper exploration of abnormal subjects. This may lead to new insights for the topographer design.

For future prototypes, it is of high importance to retrieve or create a reconstruction algorithm that can be reliably used for different surfaces (e.g., non-spherical surfaces, surface inflicted by keratoconus). Although, currently there are several techniques available, most of them require very constrained setups. Hence, having the handling of a portable device in mind, robustness must be a central part of such algorithm.

Redesigning the topographer so it can more reliably assure the repeatability of the assessment is another promising direction of future exploration. Also, the redesign would be important to improve the user experience. For instance, during our experiments, some subjects have experienced a hard time dealing with the intensity of the light, which could be simply solved by using a non-visible light.

REFERENCES

- ALKHALDI, W. **Statistical signal and image processing techniques in corneal modeling**. 2010. Thesis (Doctoral in Elektrotechnik und Informationstechnik) — Elektrotechnik und Informationstechnik, Technischen Universität Darmstadt, Darmstadt, 2010.
- ALKHALDI, W. et al. Enhancing the standard operating range of a placido disk videokeratoscope for corneal surface estimation. **IEEE Transactions on Biomedical Engineering**, Piscataway, v. 56, no. 3, p. 800-809, March 2009.
- APPLEGATE R.; HOWLAND, H. Noninvasive measurement of corneal topography. **IEEE Engineering in Medicine and Biology Magazine**, Piscataway, v. 14, no. 1, p. 30-42, Jan./Feb. 1995.
- BARSKY, B.; KLEIN, S.; GARCIA, D. Gaussian power with cylinder vector field representation for corneal topography maps. **Optometry & Vision Science**, Alphen aan den Rijn, v. 74, no. 11, p. 917-925, November 1997.
- CANEIRO, D. A.; ISKANDER, D. R.; COLLINS, M. J. Estimating corneal surface topography in videokeratometry in the presence of strong signal interference. **IEEE Transactions on Biomedical Engineering**, Piscataway, v. 55, no. 10, p. 2381-2387, October 2008.
- CARVALHO, L. A. V. d.; BRUNO, O. M. Different techniques for plácido image analysis may improve precision of videokeratography. **Arquivos Brasileiros de Oftalmologia**, São Paulo, v. 68, p. 797- 805, dezembro 2005.
- CARVALHO, L. A. V. de. A hand-held in vivo corneal topography system. **Revista Brasileira de Engenharia Biomédica**, Uberlândia, v. 12, n. 1, p. 35-42, abril 2006.
- CARVALHO, L. A. V. de; BRUNO, O. M. Spatial and frequency domain techniques for segmentation of placido images and accuracy implications for videokeratography. **Computer Methods and Programs in Biomedicine**, v. 79, no. 2, p. 111-119, August 2005.
- CHURMS, P. W. The sagitta of a toroidal surface in an oblique meridian. **Ophthalmic and Physiological Optics**, Hoboken, v. 1, no. 1, p. 29-38, November 1981.
- CORBETT, M. C.; ROSEN, E. S.; O'BRART, D. P. **Corneal topography, principles and applications**. London: British Journal of Ophthalmology, 1999.
- DOSS, J. D. et al. Method for calculation of corneal profile and power distribution. **American Academy of Ophthalmology**, San Francisco, v. 99, no. 7, p. 1261-1265, July 1981.
- FLORINDO, J. a. B. et al. Mumford-shah algorithm applied to videokeratography image processing and consequences to refractive power values. **Computer Methods and Programs in Biomedicine**, Amsterdam, v. 87, no. 1, p. 61-67, July 2007.
- FORRESTER, J. **The Eye: basic sciences in practice**. 3th ed. Philadelphia: Saunders, 2002.

GUENTER, B.; PARENT, R. Computing the arc length of parametric curves. **IEEE Computer Graphics and Applications**, Los Alamitos, v. 10, no. 3, p. 72-78, May 1990.

GUTMARK, R.; GUYTON, D. L. Origins of the keratometer and its evolving role in ophthalmology. **Survey of Ophthalmology**, Amsterdam, v. 55, no. 5, p. 481-497, Sept./Oct. 2010.

HALSTEAD, M. A. et al. Reconstructing curved surfaces from specular reflection patterns using spline surface fitting of normals. In: INTERNATIONAL CONFERENCE ON COMPUTER GRAPHICS AND INTERACTIVE TECHNIQUES , 23., 1996, New Orleans, LA. **Proceedings...** New York: ACM, 1996. p. 335-342.

HELMHOLTZ, H. von. **Helmholtz's treatise on physiological optics**. New York: The Optical Society of America, c1924.

HILMANTEL, G. et al. Accuracy with which the tms-1 can measure elevations of asymmetric surfaces. **Investigative Ophthalmology & Visual Science**, St. Louis, v. 38, no. 4, p. 3966-3966, July 1997.

JACKSON, E. Value of the ophthalmometer in practical refraction work. **Transactions of the American Ophthalmological Society**, San Francisco, v. 7, no. 1, p. 177-180, July 1894.

JONGSMA, F.; BRABANDER, J. de; HENDRIKSE, F. Review and classification of corneal topographers. **Lasers in Medical Science**, Heidelberg, v. 14, no. 1, p. 2-19, March 1999.

KLEIN, S. A. Axial curvature and the skew ray error in corneal topography. **Optometry & Vision Science**, Alphen aan den Rijn, v. 74, no. 11, p. 931-944, November 1997.

KLEIN, S. A. A corneal topography algorithm that produces continuous curvature. **Optometry & Vision Science**, Alphen aan den Rijn, v. 69, no. 11, p. 829-834, November 1992.

KLEIN, S. A. Corneal topography reconstruction algorithm that avoids the skew ray ambiguity and the skew ray error. **Optometry & Vision Science**, Alphen aan den Rijn, v. 74, no. 11, p. 945-962, November 1997.

KNOLL, H. A.; STIMSON, R.; WEEKS, C. L. New photokeratoscope utilizing a hemispherical object surface. **Optical Society of America**, New York, v. 47, no. 3, p. 221-222, March 1957.

MANDELL, R. B.; HELEN, R. S. Mathematical model of the corneal contour. **The British Journal of Physiological Optics**, London, v. 26, no. 1, p. 183-197, April 1971.

MATTIOLI, R.; TRIPOLI, N. K. Corneal geometry reconstruction with the keratronvideokeratographer. **Optometry & Vision Science**, Alphen aan den Rijn, v. 74, no. 11, p. 881-894, November 1997.

PAMPLONA, V. F. et al. Netra: interactive display for estimating refractive errors and focal range. **ACM Transactions on Graphics**, New York, v. 29, no. 4, p. 575-584, July 2010.

PAMPLONA, V. F. et al. Catra: interactive measuring and modeling of cataracts. **ACM Transactions on Graphics**, New York, v. 30, no. 4, p. 471-478, August 2011.

PINHEIRO, F. I. et al. Design and development of an ultraportable corneal topographer for smartphones as a low cost new tool for preventing blindness caused by keratoconus. **International Journal of Latest Research in Science and Technology**, Haryana, v. 4, no. 3, p. 72-76, May 2015.

PLÁCIDO, A. Novo instrumento de exploração da cornea. **Periodico d'Oftalmológica Practica**, Lisboa, v. 5, no. 1, p. 27-30, janeiro 1880.

RAMSDEN; BANKS, J. **The description of two new micrometers**. London: Royal Society of London, 1779.

RAND, R. H.; HOWLAND, H. C.; APPLGATE, R. A. Mathematical model of a placido disk keratometer and its implications for recovery of corneal topography. **Optometry & Vision Science**, Alphen aan den Rijn, v. 74, no. 11, p. 926-930, November 1997.

ROSA, A. L. B. da. **An accessible approach for corneal topography**. 2013. 79 f. Dissertação (Mestrado em Computação) - Instituto de Informática, Universidade Federal do Rio Grande do Sul, Porto Alegre, 2013.

SALMON, T. O. **Corneal contribution to the wavefront aberration of the eye**. 1999. Thesis (Doctoral in Optometry) — School of Optometry, Indiana University, Bloomington, 1999.

SCHWARTZ, S. H. **Visual perception: a clinical orientation**. 4th ed. New York: McGraw-Hill Medical, 2009.

SCHWIEGERLING, J.; GREIVENKAMP, J. Using corneal height maps and polynomial decomposition to determine corneal aberrations. **Optometry & Vision Science**, Alphen aan den Rijn, v. 74, no. 11, p. 90-916, November 1997.

SMOLEK, M. K.; KLYCE, S. D.; HOVIS, J. K. The universal standard scale: proposed improvements to the American National Standards Institute (ANSI) scale for corneal topography. **Ophthalmology**, New York, v. 109, no. 2, p. 361-369, February 2000.

YOBANI, M.-B.; DANIEL, M.-H. A review of methods for measuring corneal topography. **Optometry and Vision Science**, Alphen aan den Rijn, v. 78, no. 4, p. 240-253, April 2001.